SPECIAL
Years of the Maritime Continent
COLLECTION

Moisture Variation with Cloud Effects during a BSISO over the Eastern Maritime Continent in a Cloud-Permitting-Scale Simulation

YUNTAO WEI[a] AND ZHAOXIA PU[a]

[a] *Department of Atmospheric Sciences, University of Utah, Salt Lake City, Utah*

(Manuscript received 9 July 2020, in final form 24 March 2021)

ABSTRACT: Despite the great importance of interactions between moisture, clouds, radiation, and convection in the Madden–Julian oscillation, their role in the boreal summer intraseasonal oscillation (BSISO) has not been well established. This study investigates the moisture variation of a BSISO during its rapid redevelopment over the eastern Maritime Continent through a cloud-permitting-scale numerical simulation. It is found that moisture variation depends closely on the evolution of clouds and precipitation. Total moisture budget analysis reveals that the deepening and strengthening (lessening) of humidity before (after) the BSISO deep convection are attributed largely to zonal advection. In addition, the column moistening/drying is mostly in phase with the humidity and is related to the maintenance of BSISO. An objective cloud-type classification method and a weak temperature gradient approximation are used to further understand the column moistening/drying. Results indicate that elevated stratiform clouds play a significant role in moistening the lower troposphere through cloud water evaporation. Decreases in deep convection condensation and reevaporation of deep stratiform precipitation induce moistening during the development and after the decay of BSISO deep convection, respectively. Meanwhile, anomalous longwave radiative heating appears first in the lower troposphere during the developing stage of BSISO, further strengthens via the increase of deep stratiform clouds, and eventually deepens with elevated stratiform clouds. Accordingly, anomalous moistening largely in phase with the humidity of BSISO toward its suppressed stage is induced via compensated ascent. Owing to the anomalous decrease in the ratio of vertical moisture and potential temperature gradients, the cloud–radiation effect is further enhanced in the convective phase of BSISO.

KEYWORDS: Madden-Julian oscillation; Cloud radiative effects; Moisture/moisture budget

1. Introduction

The 20–90-day tropical intraseasonal oscillation (TISO) has strong seasonality (Lau and Waliser 2012). The wintertime TISO or the so-called Madden–Julian oscillation (MJO; Madden and Julian 1971, 1972; Zhang 2005) features a planetary-scale (Li and Zhou 2009; Wei et al. 2018) convection–circulation coupled system that propagates eastward ($\sim 5\,\mathrm{m\,s^{-1}}$) from the Indian Ocean to the western Pacific (Hendon and Salby 1994). In contrast, the boreal summer intraseasonal oscillation (BSISO) is significantly distinct from the MJO in its propagation and spatial pattern (Wang et al. 2018). Northward/eastward propagation with a northwest–southeast-tilted rainband is dominant for BSISO and prevails over the Indian–Asian summer monsoon region (Yasunari 1979; Krishnamurti and Subramanian 1982). Despite the widespread influences of TISO on global weather and climate (Zhang 2013), it is still a challenge for numerical weather and climate models to realistically simulate and accurately predict MJO (e.g., Neena et al. 2014; Jiang et al. 2015; Ahn et al. 2017) and BSISO (Sabeerali et al. 2013; Wang et al. 2019). The challenge also reflects our elusive understanding of the full dynamics intrinsic to TISO, especially the initiation of TISO events (Zhang and Yoneyama 2017; Wei et al. 2019a, 2020a).

For the two types of TISO mentioned above, MJO has been well explored. Statistically, MJO initiation can be depicted as the progressive deepening of moisture and the buildup of convective instability (Bladé and Hartmann 1993; Hu and Randall 1994; Kemball-Cook and Weare 2001). Shallow cumulus and congestus clouds dominate the cloud population and the circulation shows weak easterly winds prevailing in the lower troposphere. This process has been referred to as the ‘‘recharge’’ of MJO moist instability and generally lasts for ~15–20 days (Benedict and Randall 2007). For individual MJO episodes, the recharge process may manifest in a stepwise manner, showing alternating moistening and drying of short duration (~2–7 days; Powell and Houze 2013; Xu and Rutledge 2016). At the onset of MJO, along with the commencement of vigorously active deep convection and ‘‘westerly wind bursts’’ (WWB) in the lower troposphere and boundary layer, the upper troposphere at around 200 hPa is further moistened. Meanwhile, deep cumulonimbus clouds aggregate intensively. After the onset of deep convection, the frequency of stratiform anvil clouds increases and drying typically starts in the lower troposphere and then moves up. The disturbed atmosphere returns gradually to its normal state through the relaxation of convective instability (Benedict and Randall 2007).

Corresponding author: Dr. Zhaoxia Pu, zhaoxia.pu@utah.edu

DOI: 10.1175/JAS-D-20-0210.1

This return period usually lasts for ~25–30 days and is called the ''discharge'' of MJO.

The moisture ''recharge–discharge'' process of the wintertime MJO mentioned above has been examined extensively by budget analysis of the humidity (Benedict and Randall 2007; Hsu and Li 2012; Chikira 2014) and moist static energy (Maloney 2009; Andersen and Kuang 2012; Sobel et al. 2014; Yokoi and Sobel 2015). Possible factors contributing to the growth and decay of humidity include large-scale moisture advection, radiation, subgrid-scale microphysics, and vertical eddy transport processes (Yanai et al. 1973). In general, according to previous studies (e.g., Chikira 2014; Adames and Kim 2016), horizontal moisture advection has a damping effect and is related to the propagation of MJO, while column processes, defined as the sum of the vertical moisture advection and apparent moisture sink (Chikira 2014), are more in phase with deep convection and play a key role in destabilizing MJO. Moisture variation is also demonstrated to be closely related to cloud populations (e.g., Benedict and Randall 2007; Powell and Houze 2013; Xu and Rutledge 2014; Bellenger et al. 2015; Janiga and Zhang 2016, hereafter JZ16). However, while it is generally suggested that shallow cumulus and congestus clouds are crucial in initiating MJO through vertically convective moisture transport from the boundary layer into the lower troposphere, the role of these cumulus clouds in preconditioning deep convection has been questioned (e.g., Hohenegger and Stevens 2013; Kumar et al. 2013; Zermeño-Díaz et al. 2015). Specifically, Hohenegger and Stevens (2013) found that the presence of cumuli congestus over a given region generally does not enhance the likelihood of deep convection development. Kumar et al. (2013) found a moistening effect below 5 km before rainfall maximum, but no cumulus congestus clouds were observed at that time. Zermeño-Díaz et al. (2015) further showed that shallow clouds do provide perpetual background low-level moistening but do not prompt an increase in low-level moisture leading to rainfall peaks.

In addition, stratiform anvil clouds (Houze 1997) can also likely deepen humidity and support the initiation and further development of deep convection. Some studies have unraveled that layered stratiform clouds may support the initiation of convective rainfall through a destabilization effect beneath precipitating anvils (Fabry et al. 1993; Parker and Johnson 2004; Storm et al. 2007). Mapes (2000) proposed the first model incorporating the second baroclinic mode and also identified a stratiform instability in the coupling between waves and convection. Mapes (2000), was not aware of the moisture effect, but Kuang (2008) further included moisture in the second baroclinic mode and revealed a moisture–stratiform instability for moist equatorial waves. Kumar et al. (2013) suggested that the reevaporation of stratiform precipitation may result in a middle-tropospheric moistening that precedes rainfall peaks. Rowe and Houze (2014) found that the occurrence of peak rainfall during the Dynamics of the Madden–Julian Oscillation (DYNAMO) field campaign (Zhang and Yoneyama 2017) largely coincided with the frequent wet aggregation of an enlarged stratiform area.

To quantify the efficiency of column moistening (drying) induced by external condensational heating (evaporative cooling) through indirect upward (downward) moisture advection, Chikira (2014) introduced the parameter α under a weak temperature gradient (WTG) approximation (Sobel et al. 2001). Using this parameter, JZ16 revealed that the direct moistening of the reevaporation of stratiform precipitation is smaller than its indirect drying of cooling, thereby causing a net drying effect in the lower troposphere. This was attributed by JZ16 to the large vertical moisture gradient at that level. JZ16 also found that due to the decrease in the moisture gradient with height, the removal of moisture by ice deposition in the upper troposphere in stratiform clouds became dominant and caused drying. This suggests that the net effect of microphysical processes in stratiform clouds on column moistening/drying virtually depends on the humidity profiles related to parameter α (Chikira 2014).

The moisture variation of TISO also involves the influence of cloud–radiation feedback. Chikira (2014) suggested that although the effect of radiative warming anomalies on potential temperature is small in the lower troposphere, the effect on moisture can be amplified significantly because of the large parameter α at that level. Kim et al. (2015) showed that increased cloud and moisture could trap more longwave radiation in the air column and induce additional diabatic heating anomalies. Using cloud-resolving simulations, Wang et al. (2013, 2016) showed the profound effect of radiative feedback on MJO evolution. The complex interaction among cloud, moisture, and radiation was also referred to as ''greenhouse warming feedback'' (Kim et al. 2015). Adames and Kim (2016) used a theoretical model framework to confirm the critical role of nonlocal cloud–radiation feedback associated with stratiform anvil clouds. JZ16 pointed out that anomalous radiation warming was associated mainly with weakly and nonprecipitating clouds and could result in less subsidence and drying during the enhanced phase of MJO. More recently, Inoue et al. (2020) indicated that top-heavy vertical motion profiles, which are the most typical for TISO, could build up more moisture via stronger cloud–radiation feedback for moisture mode instability. The importance of cloud–radiation feedback in TISO dynamics has been also challenged. Lee et al. (2001), for example, found that interaction between cloud and radiation weakens simulated TISO.

Despite the many studies on TISO mentioned above, most have emphasized MJO instead of BSISO. Therefore, the life cycle of moisture related to clouds has not yet been well investigated for BSISO. Also, the roles of moisture–convection feedback and cloud–radiation effects have also been much less studied for BSISO. Nevertheless, except for the fundamental discrepancies regarding their occurrence in different seasons, the processes controlling the evolution of MJO and BSISO should be case dependent (Mei et al. 2015). For instance, using a warm pool composite analysis, a recent study by Adames et al. (2016) found that meridional moisture advection is more important in explaining the eastward-propagating MJO, while zonal advection is more important for the northward propagation of BSISO. Moreover, most previous studies on intraseasonal moisture variation considered only cases over the Indian Ocean, perhaps due to the more frequent initiation of TISO in that region (Matthews 2008). Very few studies have explored cases over the Maritime Continent (MC) (Kubota et al. 2015; Yokoi and Sobel 2015), partly due to the lack of observations.

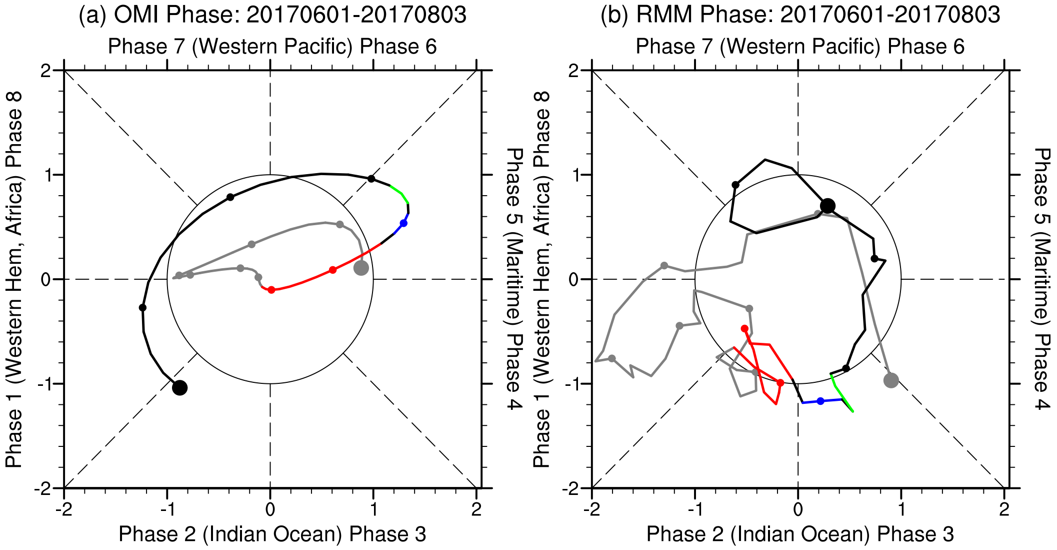

FIG. 1. (a) OMI phase diagram before (gray line) and after (black and colored lines) 1 Jul 2017. The time is marked every 5 days by circles and the first and last days are highlighted by larger gray and black circles, respectively. The colors denote the preconditioning (red), developing (blue), decaying (green), and suppressed (black) periods of this BSISO event. (b) As in (a), but for the RMM index.

Based on the above review, the purposes of this study are to investigate the moisture variation and related cloud and radiation effects during a BSISO event. We will focus on a BSISO episode occurring over the MC during July 2017. We choose this event because it features deep convection and the rapid redevelopment of precipitation upon approaching the Sulawesi Sea (see detailed description in section 2), which, however, cannot be observed from the composite BSISO (e.g., Kikuchi et al. 2012). We will address similar discoveries from MJO regarding moisture variation as well as cloud–radiation effects and interactions (Chikira 2014; JZ16), but during BSISO. A cloud-permitting-scale numerical simulation of this BSISO event is conducted by the community mesoscale Weather Research and Forecasting (WRF) Model to analyze the complex interactions among moisture, cloud, radiation, and convection.

The rest of the paper is arranged as follows. Section 2 reviews the global evolution of this BSISO event. Section 3 introduces the numerical model, simulations, and diagnostic strategy. Section 4 validates the model simulation. The moisture variation and related cloud–radiation effects are examined in sections 5 and 6, respectively. A discussion of the results and a summary of the main findings are presented in section 7.

2. Characterization of the BSISO event

We first use satellite and reanalysis data products to characterize a BSISO event during July 2017. The satellite precipitation product from the Climate Prediction Center morphing technique (CMORPH) (Joyce et al. 2004) data is available at a horizontal resolution of 8 km and a time step of 30 min. Hourly, 0.25° horizontal resolution analysis data at pressure levels from the fifth generation of the European Centre for Medium-Range Weather Forecasts (ERA5) atmospheric reanalyses (Hersbach et al. 2020) are also used. To track the convection and circulation evolution before and after the onset of this BSISO event, we also utilize daily and 2.5° interpolated outgoing longwave radiation (OLR) data from the National Oceanic and Atmospheric Administration (NOAA) satellite (Liebmann and Smith 1996) and the daily OLR-based MJO index (OMI; Kiladis et al. 2014), and the real-time multivariate MJO (RMM; Wheeler and Hendon 2004) index in June–July 2017.

Figure 1 shows phase diagrams of the OMI and RMM indexes during June–July 2017. In June, the OMI is very weak and never exceeds the unit circle (Fig. 1a), implying a weak intraseasonal-scale convection signal in this month. In addition, OMI exhibits a sharp variation centered on 15 June, which is directly caused by the quick decrease in the y-axis component related to the first empirical orthogonal function mode of 30–96-day OLR (Kiladis et al. 2014) and may correspond to a local synoptic-scale convective signal. The RMM index (Fig. 1b), which largely reflects the upper-tropospheric (~200 hPa) circulation signal (Straub 2013), indicates that the intraseasonal-scale circulation is not strong in June. One exception is 12–27 June, during which the RMM amplitude is somewhat stronger, which may reflect a local standing oscillation or simply the noisy nature of the RMM index (Roundy et al. 2009). After 25 June, the RMM phase points return to the unit circle again and display no smooth eastward propagation (i.e., anticlockwise rotation). In contrast, both the OMI and RMM indexes become strong and show a clear eastward propagation in July (especially after 10 July), indicating the significance of this BSISO event. The June–July contrast also implies that the onset of this BSISO event is likely primary (Matthews 2008).

To examine the propagation of this BSISO event in the global tropics, Fig. 2 shows Hovmöller diagrams of CMORPH precipitation, 20–100-day filtered NOAA OLR, and ERA5 850- and 200-hPa zonal wind anomalies averaged over 5°S–

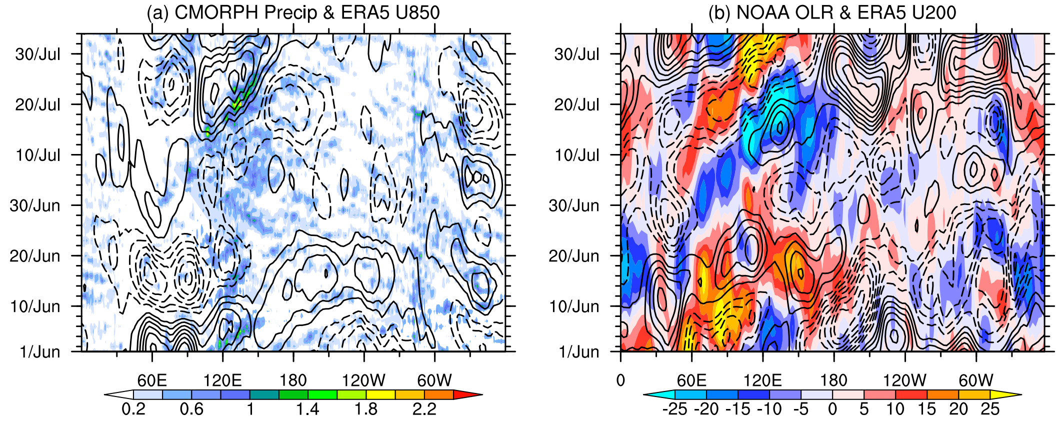

FIG. 2. (a) Hovmöller diagram of CMORPH precipitation (shading, mm h^{-1}) and ERA5 zonal wind at 850 hPa (contours, m s^{-1}). The solid (dashed) contours denote the westerly (easterly) winds, with a contour interval of 0.5 m s^{-1}. (b) Hovmöller diagram of NOAA interpolated OLR (shading, W m^{-2}) and ERA5 zonal wind at 200 hPa (contours, m s^{-1}). The solid (dashed) contours denote the westerly (easterly) winds, with a contour interval of 1 m s^{-1}. Both OLR and ERA5 data have been subjected to 20–100-day bandpass filtering. All variables are averaged over the latitudinal band between 5°S and 10°N.

10°N. The eastward propagation is initiated first from the western Indian Ocean around 30 June. Unlike in classical TISO events, the convection signal does not grow when propagating into the eastern Indian Ocean; rather, it weakens quickly (see the gap west of ~110°E). However, when it approaches the Sulawesi Sea over the eastern MC, both precipitation (Fig. 2a) and OLR (Fig. 2b) increase sharply, suggesting *the possible role of local processes such as cloud–radiation and moisture–convection feedbacks*. The lower-level westerly and upper-level easterly wind anomalies are well established. There is no circumnavigating Kelvin wave (Seo and Kim 2003), but only a locally standing signal over the equatorial Atlantic Ocean and Africa (also reflected in the OMI/RMM phase diagram; see Fig. 1), implying again that the onset of BSISO is primary. Therefore, in this study we will focus on the Sulawesi Sea to examine the moisture variation during this BSISO event.

3. WRF simulation and analysis methods

a. *WRF Model and numerical simulation*

The numerical model used in this study is the advanced research version of WRF version 4.0 (Skamarock et al. 2019). A single domain is configured with horizontal grid spacing of 3 km and 37 vertical sigma levels with the model top at 50 hPa (Fig. 3). A transition zone of five grid points is used along the lateral boundary. Microphysical processes are simulated using the WRF single-moment 6-class scheme. Subgrid-scale vertical turbulent eddy mixing is parameterized using the Yonsei University planetary boundary layer scheme. Radiative processes are calculated using the Rapid Radiative Transfer Model longwave radiation scheme and the Dudhia shortwave scheme. The cumulus scheme is turned off under the 3-km resolution. The unified Noah land surface model is used to simulate surface processes. The revised Fifth-generation

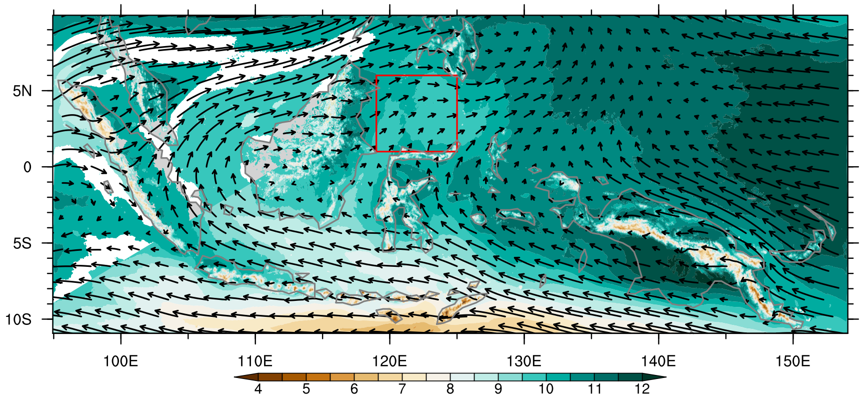

FIG. 3. WRF modeling domain. Overlaid are the mean horizontal winds (vectors, m s^{-1}) and specific humidity (shading, g kg^{-1}) averaged over 700–900 hPa during July 2017. The red rectangle shows the region used to examine the moisture–convection feedback with cloud effects during this BSISO event.

Pennsylvania State University–NCAR Mesoscale Model Monin–Obukhov scheme is used to parameterize the surface layer.

Similar to Hagos et al. (2016), we performed a set of WRF simulations initiated at 0000 UTC 1 July 2017 and integrated continuously forward to 0000 UTC 1 August 2017, during which a primary type of BSISO event occurs (Fig. 1). The initial and boundary conditions are derived from the Final (FNL) analysis data of the National Centers for Environmental Prediction (NCEP) Global Forecast System (GFS). The first three days are regarded as the spinup period. The effectiveness of different sea surface temperature (SST) products, including those from the reanalysis of NCEP FNL, ERA5, and the NOAA daily 0.25° Optimum Interpolation SST v2 (Reynolds et al. 2007), was measured as the lower boundary condition was tested. It was shown that with the ERA5 SST (see the description in Hersbach et al. 2020), the WRF Model could reproduce a reasonable BSISO simulation. Therefore, the WRF simulation driven by ERA5 SST is analyzed in this study.

b. *Analysis of moisture and heat budgets*

We introduce here the budget analysis of atmospheric humidity q and potential temperature $\theta = T(P_0/P)^{R/C_p}$, where C_p is the specific heat capacity of air at a constant pressure, T is absolute temperature (in K), R is the gas constant, P is pressure, and P_0 (=1000 hPa) is the standard reference pressure. Following Yanai et al. (1973) and Tao et al. (1993), the conservation equations of q and 0 can be written at a constant pressure level p:

$$\frac{\partial\overline{q}}{\partial t} + \overline{\nabla\cdot q\mathbf{V}} + \frac{\partial\overline{q}\,\overline{\omega}}{\partial p} = (\overline{e} - \overline{c}) - \frac{\partial\overline{q'\omega'}}{\partial p} \equiv -\frac{Q_2}{L_v}, \tag{1}$$

$$\overline{\pi}\left[\frac{\partial\overline{\theta}}{\partial t} + \overline{\nabla\cdot\theta\mathbf{V}} + \frac{\partial\overline{\theta}\,\overline{\omega}}{\partial p}\right] = L_v(\overline{c} - \overline{e}) + \overline{Q_R} - \overline{\pi}\left[\frac{\partial\overline{\theta'\omega'}}{\partial p}\right] \equiv Q_1, \tag{2}$$

where ω is the averaged vertical p velocity, $\mathbf{V}$ is the horizontal wind vector, Q_R is the radiative heating rate, and $\overline{\pi} = (P/P_0)^{R/C_p}$ is the Exner function representing nondimensional pressure. The overbars denote the horizontal average, and primes indicate deviations from the horizontal average; c and e are the rates of condensation and evaporation, respectively; L_v is the latent heat of vaporization. The values of Q_1 and Q_2 (the apparent heat source and moisture sink, respectively) are calculated indirectly as the sum of the left-hand side of Eqs. (1) and (2). Following Chikira (2014), we refer to all vertical processes with regard to moisture variation as column process M_C, which includes large-scale vertical moisture advection M_V ($=-\overline{\omega}\partial\overline{q}/\partial p$) and the total effect of subgrid-scale microphysics and the eddy diffusion process M_{ME} ($=-Q_2/L_v$). Accordingly, we may rewrite the moisture tendency $\partial\overline{q}/\partial t$ equation as follows:

$$\partial\overline{q}/\partial t = M_H + M_C = M_H + M_V + M_{ME}, \tag{3}$$

where M_H ($=-\overline{\mathbf{V}}\cdot\nabla\overline{q}$) is the horizontal advection and M_C ($=M_V + M_{ME}$) is the so-called column process effect.

c. *Classification of cloud types*

To examine the cloud-related column-moistening and column-drying effects, a modified cloud-type classification method from Churchill and Houze (1984) and Shige et al. (2004) is adopted here. In contrast to JZ16, who identified cloud populations using only reflectivity, this method instead incorporates rain rate, vertical profiles of vertical velocity, and mixing ratios of cloud water and rainwater. The method identifies grid points with a surface rain rate 2 times larger than the value of the background average as deep convective (DC) cores. Points with a surface rain rate larger than 20 mm h^{-1} are also treated as DC points. The background value here is defined as the box-averaged rain rate of 30 × 30 km^2. All other points with nonzero surface precipitation are designated as deep stratiform (DS). Sensitivity tests showed that more DC with less shallow rain and fewer DS grid points will be identified with increasing background area size. Nevertheless, the main results of this study remain under a large range of background area sizes from 18 × 18 km^2 to 78 × 78 km^2.

For grid points without surface precipitation, elevated precipitation points (such as the tilted updrafts and new cells ahead of a convective line) (Tao et al. 1993) are identified as those where there is no positive rainwater mixing ratio anywhere in the column. Of the elevated precipitation points, two extra criteria are applied to identify DC points: cloud water mixing ratio exceeding 0.5 g kg^{-1} or updraft exceeding 3 m s^{-1} below the melting level (or 0°C freezing level). Otherwise, they are classified as elevated stratiform (ES). Finally, DS points are reassigned as shallow cloud (SC) rain points if the cloud water mixing ratio is larger than 0.03 g kg^{-1} between 500 and 2000 m height, in contrast to Shige et al. (2004), who identified SC points using the precipitation-top height. Since the cloud-permitting scale of 3 km used in this study is still too coarse to resolve cumulus-scale shallow convection, we do not further classify the SC points as shallow convective or shallow stratiform, partly because the two SC rain points share highly similar diabatic heating and moistening profiles (Vincent and Lane 2018).

Using this cloud-type classification method, we identified all four types (i.e., DC, DS, ES, and SC) in the model domain and tracked their time evolution. In this way, the influence of a cloud type on any variable related to updrafts or downdrafts, such as surface rain rate, vertical velocity, diabatic heating and moistening profiles, and column processes, can be isolated explicitly. We tracked the evolution of these variables averaged over the BSISO redevelopment region (1°–6°N, 119°–125°E) to explore the role of different moistening/drying effects induced by different cloud types in the moisture variation of this BSISO event. We also checked the moisture processes over the cloud-free area for this BSISO event, but they were negligible and weak and thus were not analyzed in this study.

4. Simulation validation: Wind and precipitation evolution

We first compare the mean rain rate during July between WRF and CMORPH in Figs. 4a and 4b. High precipitation is

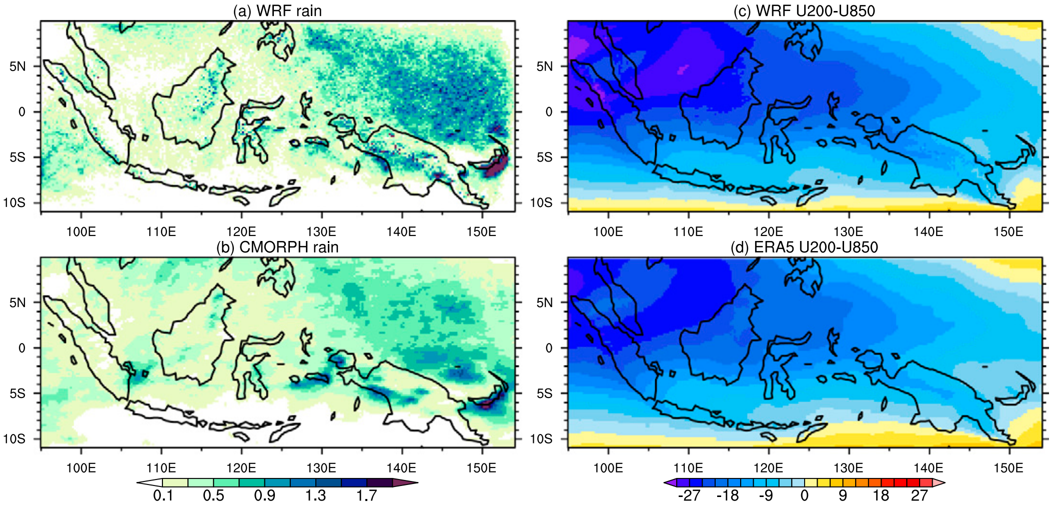

FIG. 4. July-mean rainfall (mm h^{-1}) from the (a) WRF simulation and (b) CMORPH. Difference in July-mean zonal wind between 200 and 850 hPa (m s^{-1}) from the (c) WRF simulation and (d) ERA5.

observed mainly north of the equator in CMORPH (Fig. 4b), reflecting the seasonal march of the thermal equator. The spatial distribution of the rainfall maxima (such as those over the equatorial Indian Ocean, the western Pacific Ocean, and the coastal and island regions of Borneo, Sulawesi, New Guinea, and New Britain) generally resembles the July-mean climatology (Ricko et al. 2016). An organized, large-scale pattern in precipitation is especially evident over the western Pacific Ocean, which is closely related to the redevelopment of BSISO. Strong easterly vertical wind shear centered at 5°N is seen over the Asian summer monsoon region (Fig. 4d) and plays a key role in contributing to the northward shift of BSISO deep convection through the generation of barotropic vorticity (Jiang et al. 2004). Comparison with CMORPH rainfall and ERA5 products shows that the WRF Model reasonably simulates the spatial patterns of precipitation (Fig. 4a) and vertical wind shear (Fig. 4c) while overestimating their amplitudes.

Figures 5a and 5b compare Hovmöller diagrams of daily mean precipitation averaged over 1°–6°N between the WRF simulation and CMORPH. The WRF simulation agrees well with the satellite data in representing the BSISO event, such as the sudden increase in precipitation over the Sulawesi Sea around 16 July and the slow eastward propagation with a phase speed of ~3.8 m s^{-1}. Propagation of BSISO into the western Pacific Ocean well explains the large-scale pattern of July-mean precipitation there (Fig. 4). High-frequency variation is apparent in the hourly precipitation (Figs. 5c,d). Fast westward-propagating (~10.7 m s^{-1}) signals are clearly represented in both CMORPH and the WRF simulation. Some of those become more prominent in the active phase of BSISO along the path of large-scale eastward propagation. Additionally, the fast eastward-propagating (~8.5 m s^{-1}) precipitation signals are also evident, especially over Sumatra (~100°E) and Borneo (~120°E). Compared with CMORPH data (Fig. 5d), the WRF simulation displays stronger amplitude in these signals, which is common in cloud-permitting models (e.g., Vincent and Lane 2016, 2018; Wei et al. 2020b) when compared with satellite observations. Based on previous studies, the westward-propagating signals are virtually 2-day equatorial waves (Chen and Houze 1997; Tulich and Kiladis 2012), while the fast eastward-propagating signals are diurnal gravity waves locked with local topography (Ruppert and Zhang 2019; Ruppert et al. 2020).

The spatial and temporal evolution of 800-hPa zonal wind (U800 hereafter) simulated by the WRF Model agrees well with ERA5 (Figs. 5a,b). U800 and rainfall display a phase relation similar to that in the conceptual model originally depicted by Madden and Julian (1972); namely, the rainfall maximum is well collocated with the intersection of low-level easterlies and westerlies, with the former leading and the latter trailing the convective center. As expected from the profound easterly wind shear shown in Fig. 4, alternating westerly and easterly winds coupled with enhanced and suppressed rainfall propagating westward are obvious east of ~119°E. The areas of westward- and eastward-propagating synoptic rainfall signals correspond well with the large-scale easterly and westerly background winds at 800 hPa, respectively, suggesting the modulation of the large-scale wind advection effect (Wei et al. 2020b). After 17 July, the lower-level wind over the BSISO redevelopment region (outlined by the two vertical black lines in Fig. 5) is dominated by a westerly in both WRF and the ERA5 and is associated mainly with the equatorial Rossby wave response to the BSISO deep convection over the western Pacific (Gill 1980).

A unique characteristic of BSISO, its northward propagation, is also examined. Figure 6 shows the daily mean precipitation averaged over the longitudinal range of 120°–140°E from WRF and CMORPH. In CMORPH (Fig. 6b), the precipitation is distributed mainly north of ~6°S, consistent with Fig. 4c. The space–time evolution shows an evident increase and a large-scale organization in precipitation after 15 July, which corresponds well with the sharp redevelopment of BSISO over the Sulawesi Sea. Moreover,

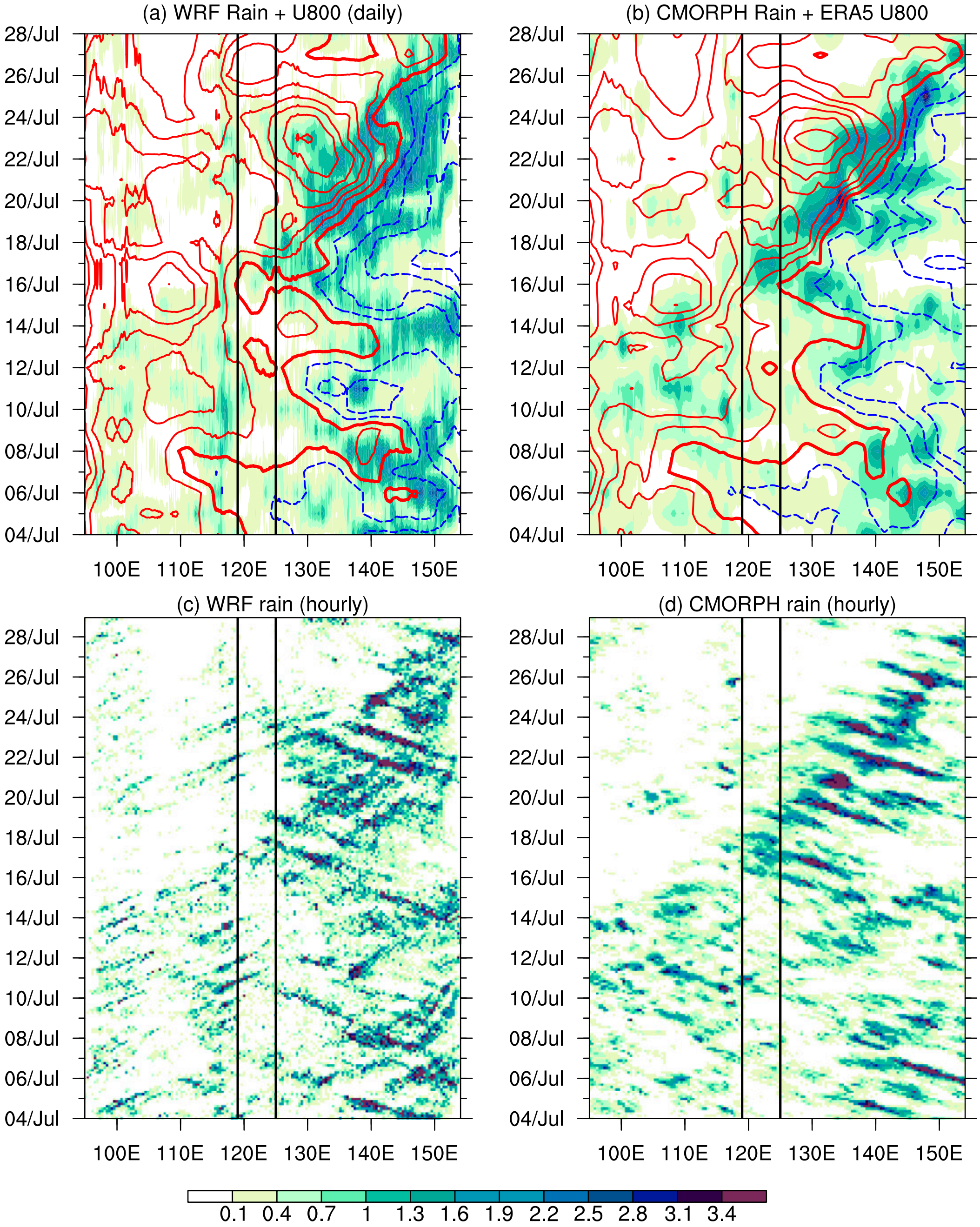

FIG. 5. Hovmöller diagram of daily mean rainfall (shading, mm h^{-1}) and 800-hPa zonal wind (contours, m s^{-1}) from the (a) WRF simulation and (b) CMORPH + ERA5 averaged over the latitudinal band of 1°–6°N. Solid red (dashed blue) contours denote westerly (easterly) winds (contour interval: 2 m s^{-1}), and zero contours are highlighted by the thick red lines. (c),(d) As in (a) and (b), but for hourly rainfall. The two vertical black lines outline the longitudinal location of BSISO redevelopment (119°–125°E).

the large-scale precipitation exhibits a clear northward propagation with a phase speed of ~1.79° day^{-1}, which is somewhat faster than the composite BSISO (~1.2° day^{-1}; Yang et al. 2020) and may reflect the case-dependent characteristics of TISO. This spatial and temporal evolution of precipitation is generally replicated with high fidelity by the WRF Model (Fig. 6a). The simulation bias involves mainly a slower northward phase propagation in WRF (~1.38° day^{-1}) as compared with CMORPH.

5. Characteristics of moisture variation

Results in the previous section indicate that the BSISO event is well simulated by the WRF Model. To further

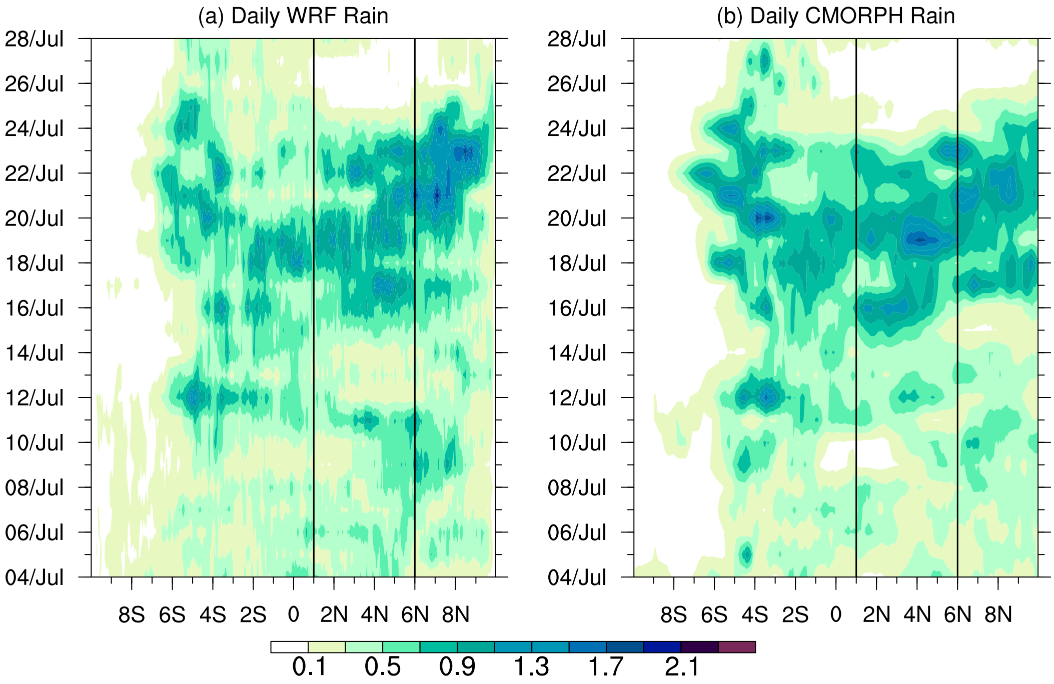

FIG. 6. Latitude–time diagram of daily mean rainfall (mm h^{-1}) from (a) the WRF simulation and (b) CMORPH averaged over the longitudinal range of 120°–140°E. The two vertical black lines outline the latitudinal location of BSISO redevelopment (1°–6°N).

characterize the BSISO event, we partition its entire life cycle into four stages, namely, the preconditioning (6–14 July), developing (15–18 July), decaying (19–22 July), and suppressed (23–28 July) stages (see the colors in Fig. 1 and further explanation, as follows).

a. Evolution of moistening and heating associated with BSISO

According to Eqs. (1)–(3), Fig. 7 shows the daily mean specific humidity (q) anomaly, vertical p-velocity (Omg) anomaly, apparent heat source (Q_1), and apparent moisture sink (Q_2) from the WRF simulations averaged over the BSISO redevelopment region, along with the daily mean precipitation from WRF and CMORPH. In the preconditioning stage, both the WRF simulation and CMORPH data show two synoptic-scale precipitation episodes with weak amplitudes. As shown in Figs. 5a and 5b, these two episodes virtually correspond to two westward-propagating precipitation signals emanating from the western Pacific Ocean. For q, a moister (drier) than normal condition is seen below (above) ~600 hPa (Fig. 7a), suggesting that the air column is becoming unstable. Omg manifests as a shallow and weak ascent anomaly in the lower level and a strong descent anomaly in the upper level (Fig. 7b). Both Q_1 and Q_2 show two local heating maxima that well coincide with the two synoptic-scale precipitation peaks. Note that for the MJO case diagnosed by JZ16, the negative Q_2 due to physical processes is greater and aggregates below 800 hPa (see their Fig. 4f), implying the key role of shallow cumuli. For the BSISO event diagnosed here, however, positive Q_2 is dominant at this stage, suggesting its drying effect through condensation. As a consequence, lateral exchange between columns through horizontal advection may be essential in causing a premoistening effect in the lower troposphere prior to the onset of BSISO deep convection (see the analysis in section 5b).

In the developing stage after 13 July, the lower-tropospheric moisture grows much faster and quickly reaches a peak in 4 days. In addition, the moistening layer is elevated further, with the top even approaching the tropopause (above 200 hPa). The combination of these two factors creates strong unstable stratification in the column, thereby prompting the occurrence of deep convection (Fig. 7b) and high precipitation in this stage. The vigorous formation of rainwater and the penetration of deep convection produce a "top-heavy" diabatic heating profile in Q_1 primarily through condensation [Eq. (2)]. In contrast to Q_1 with a maximum at ~500 hPa, Q_2 exhibits a maximum at a much lower level (~650 hPa). Compared to the shallow and weak synoptic-scale Q_1 and Q_2, the intraseasonal-scale Q_1 and Q_2 for BSISO are much deeper and stronger. Note that the humidity at this stage is already beginning to decrease from the boundary layer.

During the decaying stage from 18 to 22 July, the moisture content in the column is largely reduced, especially in the lower troposphere. Therefore, the atmosphere begins to stabilize and the precipitation area shrinks rapidly. Moreover, the vertical structures of Omg, Q_1, and Q_2 transform from a convective-like mode to a stratiform-like mode, i.e., heating/drying and ascent motion remain in the upper level while cooling/moistening and weak subsidence motion appear in the lower level. These large-scale variations in moisture and convection during the first three stages of this BSISO event coincide well with the

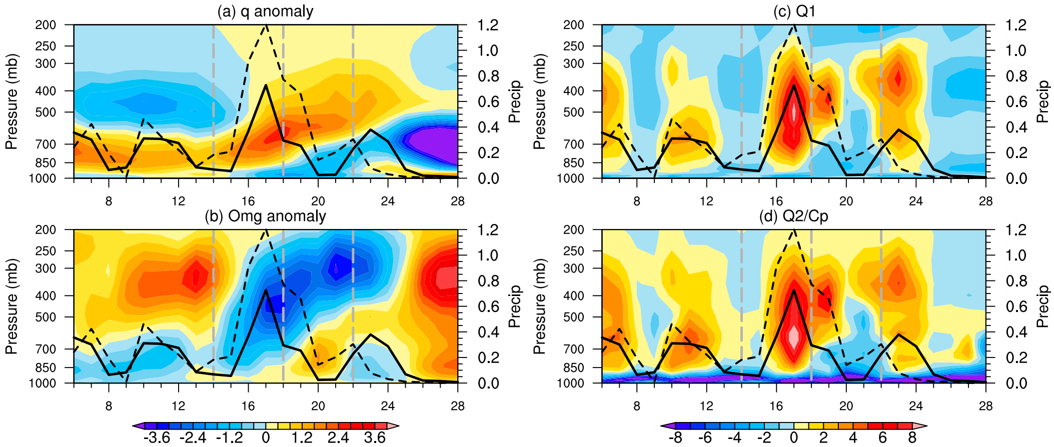

FIG. 7. Time series of the daily mean (a) specific humidity (q) anomaly (g kg^{-1}), (b) vertical pressure velocity (Omg) anomaly (hPa h^{-1}), (c) apparent heat source (Q_1, K day^{-1}), and (d) apparent moisture sink (Q_2/C_P, K day^{-1}) averaged over the region of BSISO redevelopment (1°–6°N, 119°–125°E) from the WRF simulation. All variables are subjected to a 5-day running mean to highlight intraseasonal variation. Solid and dashed lines show the daily mean precipitation (mm day^{-1}, refer to the right axis) from the WRF simulation and CMORPH data, respectively. The four BSISO periods are separated by the three vertical dashed lines.

classical paradigm of MJO built from the statistical regression and composite analysis documented in previous studies: weak and shallow convection followed by strong and deep convection and finally a stratiform-like mode (e.g., Johnson et al. 1999; Kiladis et al. 2005; Mapes et al. 2006; Benedict and Randall 2007; Haertel et al. 2008; Kiladis et al. 2009).

During 21–23 July, another synoptic precipitation episode occurs. In the WRF simulation, the peak of this precipitation episode is somewhat stronger and occurs 1 day later, as compared with CMORPH. Interestingly, a three-layer structure can be found in the profiles of the q and Omg anomalies, where drying and descent motion appear around the lower and middle troposphere, sandwiched by moistening and ascent below and aloft, respectively. The maximal heating in Q_1 and Q_2 is even higher than the deep stratiform during the transition from the decaying to the suppressed stage, suggesting a stronger cloud–radiation feedback with more ''top-heavy'' structures (Inoue et al. 2020). Analysis in section 6 will show that this deep structure is associated mainly with ES anvil clouds. After 23 July during the suppressed stage of this BSISO event, the air column becomes extremely dry and precipitation decreases to zero along with the prevalence and persistence of large-scale subsidence (Fig. 7b). Both Q_1 and Q_2 become small and even negative for Q_1.

b. *Moisture budget*

To quantify the moisture variation, we calculate the temporal tendency of specific humidity, $\partial\overline{q}/\partial t$ (refer to Fig. 8a and the black curves in Fig. 9). Consistent with the anomalous variation of q, positive $\partial\overline{q}/\partial t$ or moistening also displays a trend of deepening and strengthening in the composite manner from the preconditioning to the developing stages of BSISO (Figs. 9a,b). In the day-to-day variation of $\partial\overline{q}/\partial t$, however, an alternating moistening/drying effect can be found during the two stages (Fig. 8a), reflecting the stepwise progression toward the rainfall peak in the increasing moisture layer (Powell and Houze 2013; Johnson and Ciesielski 2013; Zermeño-Díaz et al. 2015). Negative $\partial\overline{q}/\partial t$ or drying above 900 hPa occurs first during the developing stage and then becomes deep and strong during the decaying and suppressed stages (Figs. 8a and 9b–d). In the boundary layer below 900 hPa, the temporal variation of anomalous moisture tends to lead that in the free troposphere aloft.

We further diagnose the total moisture budget (Figs. 8b,c). At first glance, M_H and M_C have an almost opposite pattern. For example, M_H displays a strong drying effect beginning early in the developing stage and tilting toward the suppressed stage of BSISO, while for M_C a moistening effect with a similar tilt is seen. Further decomposition indicates that the zonal component is one order of magnitude stronger than the meridional component of M_H (figure not shown). In addition, M_H seems to be more orthogonal with the anomalous q (i.e., moistening is leading and drying is trailing the maximum humidity), while M_C is more in phase with the anomalous q (i.e., maximum or minimum moistening corresponds to the maximum or minimum humidity). This suggests that M_H contributes mainly to the phase propagation of this BSISO event, while the growth and decay of the moisture and convection result primarily from M_C, consistent with the results of statistical analysis (Chikira 2014; Adames et al. 2016; Jiang et al. 2018). This also implies that the MJO ''moisture mode'' theory (Adames and Kim 2016; Zhang et al. 2020) may also be suitable for BSISO, although previous studies have emphasized mostly the dynamic effects (Wang and Xie 1997; Jiang et al. 2004; DeMott et al. 2013).

To quantitatively compare the relative contributions of M_H and M_C to the moisture variation, we calculate the averaged M_H and M_C in different BSISO stages (red and blue curves in Fig. 9). As seen in Figs. 9a and 9b, the deepening and strengthening of positive $\partial\overline{q}/\partial t$ during the first two stages of

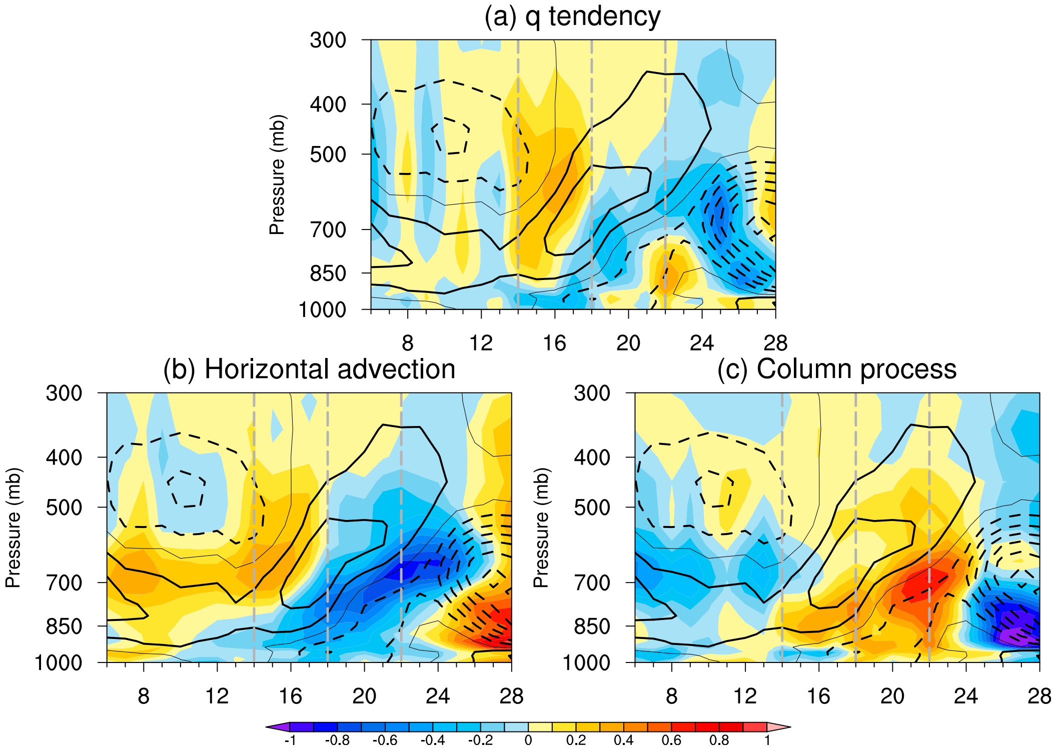

FIG. 8. As in Fig. 7, but for the (a) moisture tendency ($\partial\bar{q}/\partial t$, g kg^{-1} day^{-1}), (b) horizontal moisture advection (M_H, g kg^{-1} day^{-1}), and (c) column processes (M_C, g kg^{-1} day^{-1}). Contours show the 5-day running-mean specific humidity anomalies (g kg^{-1}), where positive (negative) anomalies are represented by solid (dashed) contours and zero contours are highlighted by thin lines; the contour interval is 0.2 g kg^{-1}.

BSISO are attributed mainly to M_H (red curves), and M_C (blue curves) induces a strong moistening only below 700 hPa, which is partially reduced by the drying of M_H. This suggests that the trigger of deep convection in this BSISO event is more sensitive to horizontal advection than to column processes, which tends to be contrary to MJO (Hagos et al. 2014; Powell and Houze 2015). Drying occurring first below 850 hPa during the developing stage is also due to M_H being balanced by M_C. During the decaying stage, the much-strengthened negative M_H throughout the column overwhelms the positive M_C, leading to a deepened and strengthened drying effect centered at ~700 hPa (Fig. 9c). At the suppressed stage, the drying

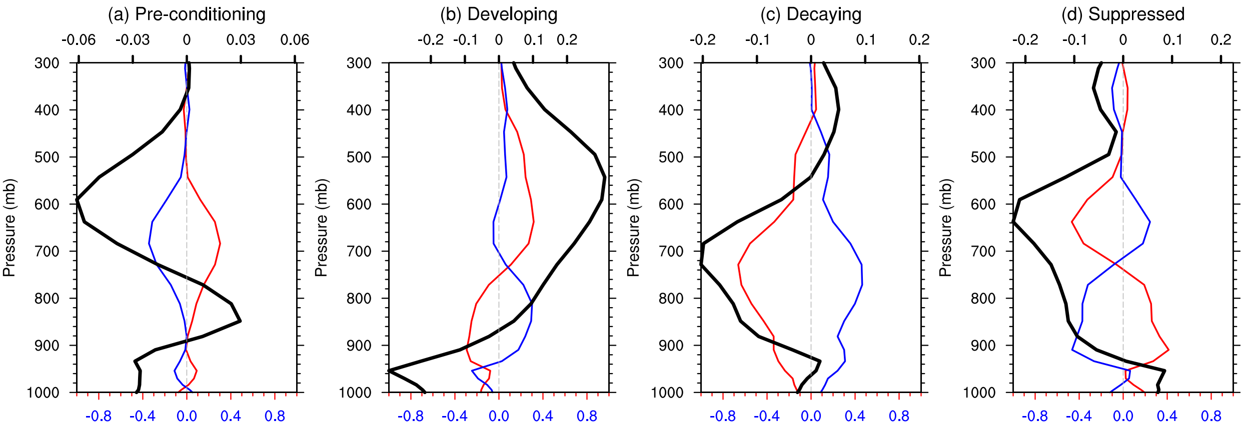

FIG. 9. Composite vertical profiles of moisture budget terms during the (a) preconditioning, (b) developing, (c) decaying, and (d) suppressed period of this BSISO event. Moisture tendency ($\partial\bar{q}/\partial t$, black; refer to the top axis), horizontal moisture advection (M_H, red; refer to the bottom axis), and column processes (M_C, blue; refer to bottom axis). Note the different ranges of the top axes in the different BSISO periods.

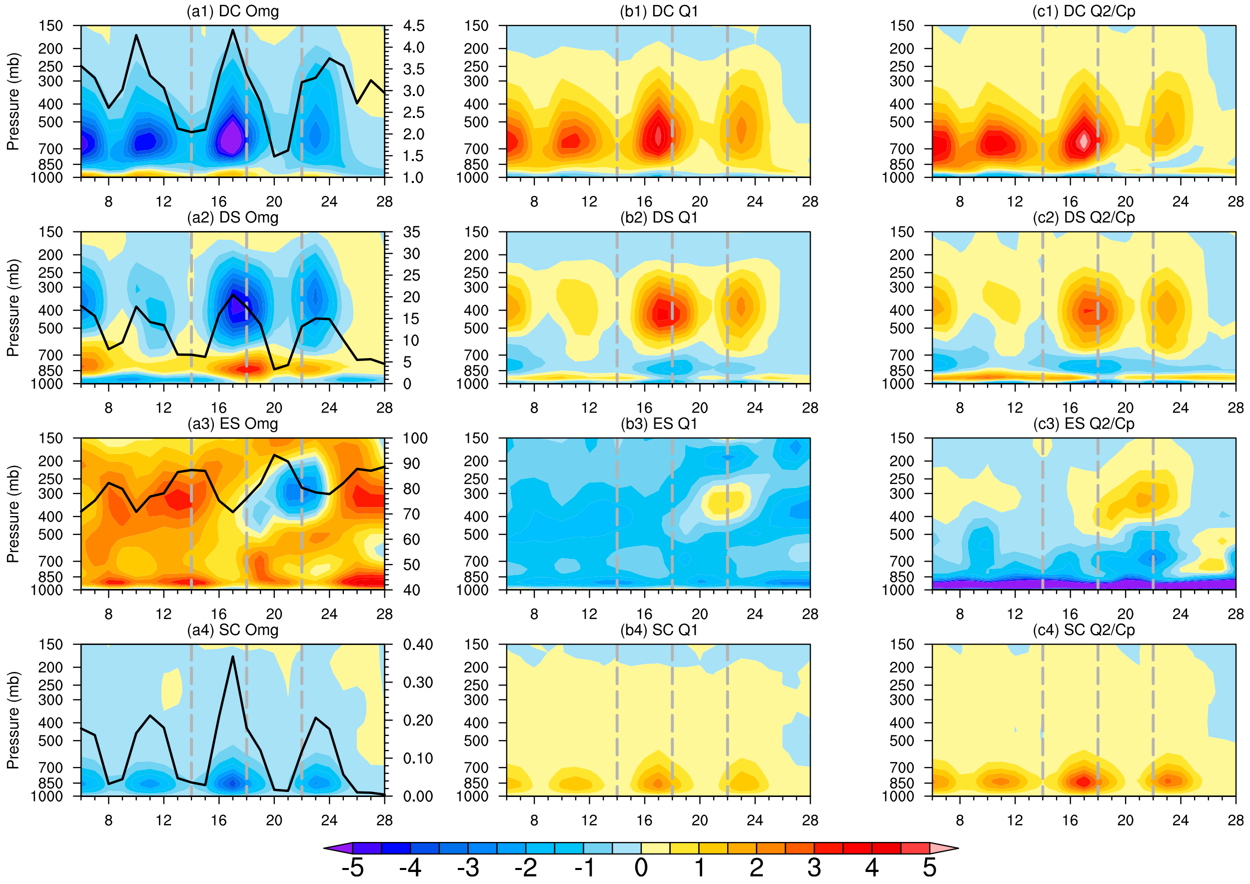

FIG. 10. Time evolution of the vertical profiles of daily mean (left) Omg (hPa h^{-1}), (center) Q_1 (K day^{-1}), and (right) Q_2/C_P (K day^{-1}) averaged over the [a(1)],[b(1)],[c(1)] deep convective (DC), [a(2)],[b(2)],[c(2)] deep stratiform (DS), [a(3)],[b(3)],[c(3)] elevated stratiform (ES), and [a(4)],[b(4)],[c(4)] shallow-cloud (SC) areas. The black line overlaid in the left panel shows the daily mean area fraction (%; refer to the right axis) of [a(1)] DC, [a(2)] DS, [a(3)] ES, and [a(4)] SC. The four BSISO periods are separated by the three vertical dotted lines.

center is elevated further to ~600 hPa by M_H, while the drying below ~750 hPa results from the negative M_C anomaly balanced by the positive M_H anomaly.

6. Cloud effects

While section 5 has demonstrated the critical role of horizontal advection in recharging and discharging BSISO moisture, column processes are more related to the maintenance of BSISO moisture and convection. Here, we further examine the relationship between column moistening/drying and cloud effects using the output of the cloud-permitting WRF simulation.

a. Column moistening/drying by cloud type

We first look at the variation in different cloud populations and their corresponding vertical motion and diabatic heating profiles. Figure 10 shows the time evolution of daily mean Omg, Q_1, and Q_2 averaged over the areas of DC, DS, ES, and SC along with their daily mean area fractions (black lines in left panel). As seen in Figs. 10a(1), 10b(1), and 10c(1), DC manifests as a vertical structure of deep ascent accompanied by deep heating and drying in Q_1 and Q_2. In contrast, SC shows a much shallower maximum in these three parameters [Figs. 10a(4),b(4),c(4)]. For DS, a vertical dipolar structure is obvious: subsidence and cooling/moistening below the melting level (~600 hPa), and ascent and heating/drying aloft [Figs. 10a(2),b(2),c(2)]. For ES, a dipolar structure like that for DS but with an elevated node is visible only during the transition from the decaying to the suppressed stages of BSISO; otherwise it displays no well-defined structure [Figs. 10a(3),b(3),c(3)]. These diabatic heating and vertical motion profiles of different cloud types are largely consistent with previous studies (Schumacher et al. 2004, 2007; Zhang and Hagos 2009; Funk et al. 2013; Handlos and Back 2014), indicating the effectiveness of the cloud-type classification method.

As a result of the consistent variation in their area fractions, DC, DS, and SC show a similar time evolution in the strength of vertical motion and diabatic heating. For example, the ascent and heating for all three cloud types reach a peak later in the developing period of BSISO. This suggests that SC, DC, and DS are the strongest in the mature phase of BSISO,

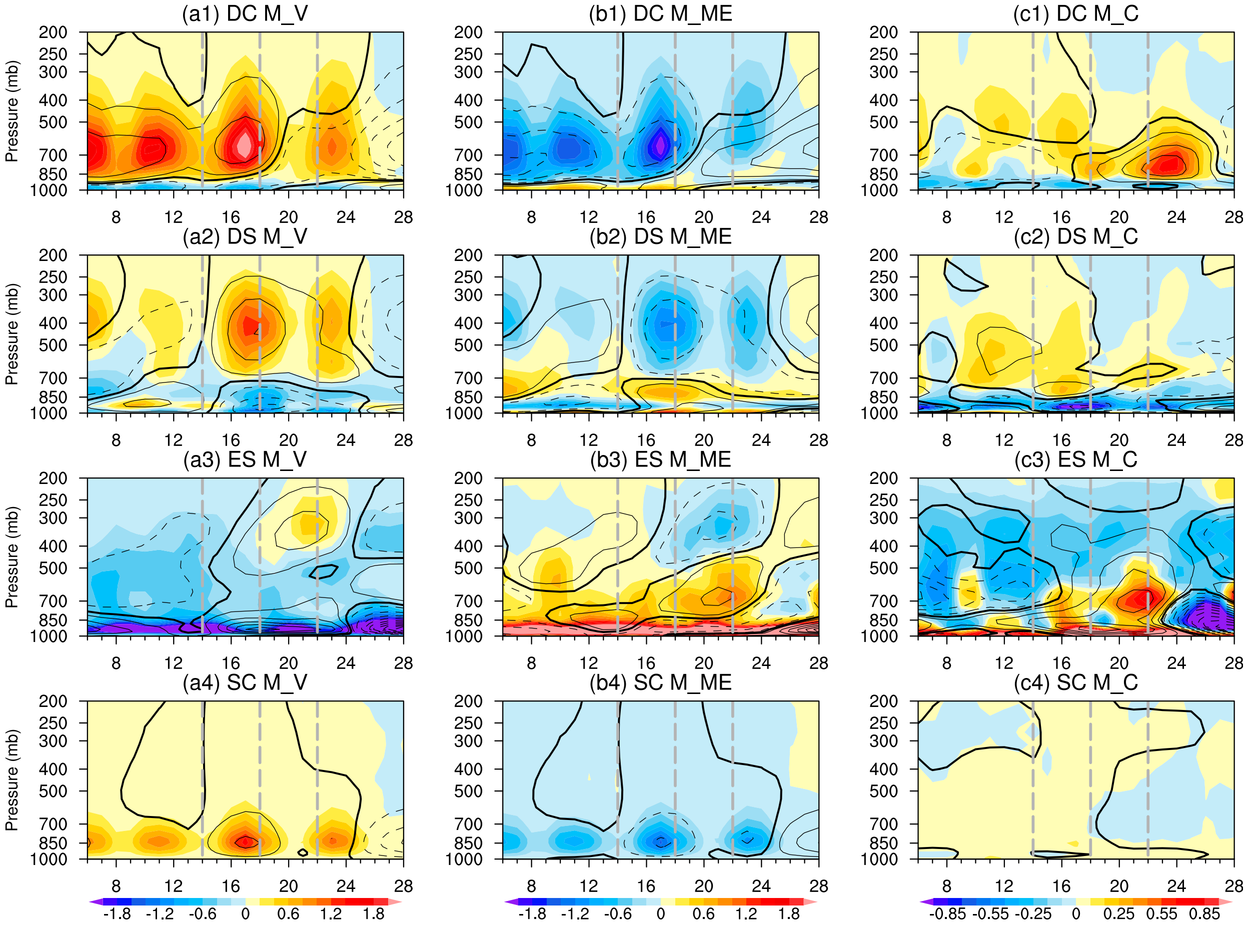

FIG. 11. Time evolution of the vertical profiles of daily mean (left) vertical moisture advection M_V, (center) total effect of microphysical and eddy processes M_{ME}, and (right) column processes M_C averaged over the [a(1)],[b(1)],[c(1)] DC, [a(2)],[b(2)],[c(2)] DS, [a(3)],[b(3)],[c(3)] ES, and [a(4)],[b(4)],[c(4)] SC areas. The contours show the 5-day running-mean anomalies, with positive (negative) anomalies denoted by solid (dashed) contours. The zero values are highlighted by thick contours. The four BSISO periods are separated by the three vertical dotted lines.

supporting the "building block" perspective proposed by Mapes et al. (2006). For ES, however, the maximum occurs during the transition from the decaying to suppressed stages of BSISO, which coincides well with the synoptic-scale precipitation event and the very top-heavy heating profiles on 21–23 July (Fig. 7). The opposite variation of ES with other cloud types is very similar to that of weakly/nonprecipitating clouds identified by JZ16, who found that those clouds were associated mainly with radiation feedback. Our analysis in the next subsection indicates that the ES anvil clouds indeed play a similar role. With these variations in vertical motion and diabatic heating profiles in mind, we now analyze and explain the column moistening and drying related to convective clouds and then stratiform anvil clouds.

Figure 11 shows the time evolution of vertical profiles in M_V, M_{ME}, and M_C along with their anomalies averaged over different cloud areas. As expected from the vertical profile of Omg [Fig. 10a(1)], the M_V of DC always shows a deep moistening in the free troposphere and drying in the boundary layer [Fig. 11a(1)]. An opposite pattern is seen for M_{ME} [Fig. 11b(1)]. In the boundary layer, the descent-induced drying overcomes the moistening of M_{ME}, thereby causing a net drying [Fig. 11c(1)]. In the free troposphere, M_V and M_{ME} generally cancel out during the first two stages of BSISO, which induces a weak amplitude in the total M_C and therefore a negative M_C anomaly relative to the July mean [Fig. 11c(1)]. However, after the decay of BSISO deep convection, the M_C anomaly becomes strongly positive, especially around 21–24 July because of the largely weakened M_{ME}. Besides DC, SC also induces evident M_V [Fig. 11a(4)] and M_{ME} [Fig. 11b(4)] in the boundary layer below ~700 hPa, but their net effects (i.e., summation) are negligibly small [Fig. 11c(4)] compared with DC, implying a minor role of SC in influencing the moisture variation of BSISO. This is contrary to JZ16, who demonstrated the crucial role of SC in preconditioning the passage of MJO, which was closely related to the dominance of negative Q_2 aggregating in the lower troposphere. However, in our simulation of BSISO, a positive Q_2 is dominant preceding the onset of BSISO deep convection, reflecting the weak SC moistening and therefore the negligible role of SC.

Next, we analyze the stratiform anvil clouds. By comparing Figs. 8c and 11c(3), we can see that the ES-induced anomalous M_C pattern bears a strong resemblance to the total M_C anomaly during the entire life cycle of BSISO, suggesting the major role of ES. The evolution of anomalous M_C below 800 hPa is caused mainly by M_V [Fig. 11a(3)] balanced by M_{ME} [Fig. 11b(3)]. During the transition from the decaying to the suppressed stages of BSISO, the increase in the ES area fraction causes enhanced M_{ME}, probably due to evaporation of cloud water, and therefore the anomalous M_C is strong around 21–23 July. Besides the microphysical processes, ES can also induce anomalous moistening by reducing longwave radiative cooling (see analysis in section 6b). The anomalous column drying [Fig. 11c(3)] in the preconditioning and suppressed stages of this BSISO event is attributed to the strong descent over the ES area [Fig. 10a(3)]. DS also induces anomalous M_C, with strong amplitude in the boundary layer below ~850 hPa [Fig. 11c(2)], which results mainly from M_V [Fig. 11a(2)] being balanced by M_{ME} [Fig. 11b(2)]. Above 850 hPa, however, the anomalous M_C is weak and generally shows a moistening effect. For example, during the developing stage of this BSISO event, the reevaporation of DS precipitation causes a net moistening effect over 700–850 hPa.

Overall, the results in this subsection reveal the major role of ES in the column moistening and drying for this BSISO event. The descent of ES causes drying during the preconditioning and suppressed stages of BSISO, while cloud water evaporation of ES causes moistening from the developing to decaying stages of BSISO. DC causes a strong moistening effect after the decay of BSISO deep convection mainly through the relaxation of condensation. DS enhances the M_H-induced drying through descent below 850 hPa while producing a moistening effect aloft (700–850 hPa) through the reevaporation of precipitation. The role of SC is minor in regulating the moisture variation of this BSISO event.

b. *Cloud–radiation effect under WTG approximation*

In the deep tropics, the Rossby radius of deformation of atmospheric motion is very large due to the smallness of the Coriolis parameter. Consequently, temperature disturbances can quickly spread far under the adjustment due to internal gravity waves. This leads to an important assumption in tropical dynamics, namely, the WTG approximation (Sobel et al. 2001). It assumes that the temporal and horizontal variations in air temperature are generally negligible at time scales longer than one day (Yano and Bonazzola 2009). Therefore, with the WTG approximation, one can easily derive the vertical motion driven by different sources of diabatic heating, namely, the parameterized dynamics (Wang et al. 2013, 2016). Here, we use the WTG approximation to examine the intraseasonal-scale moisture variation related to cloud–radiation feedback. Following Chikira (2014) and JZ16, using Eq. (2), a diabatic balance under the WTG approximation can be derived as follows (considering only radiation):

$$\overline{\pi}\left[\overline{\omega_R}\frac{\partial\overline{\theta}}{\partial p}\right] = \overline{Q_R}, \qquad (4)$$

where $\overline{\omega_R}$ denotes the compensated vertical motion induced by radiative heating/cooling, which can be formulated further as $\overline{\omega_R} = 1/\overline{\pi}(\partial\overline{\theta}/\partial p)^{-1}\overline{Q_R}$. Subtracting this into Eq. (1), we obtain the radiation-related vertical moisture advection

$$M_{V\_\mathrm{QR}} = \alpha\overline{Q_R}, \qquad (5)$$

where $\alpha = -1/\overline{\pi}(\partial\overline{q}/\partial p)(\partial\overline{\theta}/\partial p)^{-1}$ is an efficiency parameter that measures the amount of large-scale vertical moisture advection induced by a given radiative heating rate (Chikira 2014). Following JZ16, we use the α averaged over the BSISO redevelopment region to calculate M_{V_QR}. When we consider shortwave and longwave radiation, Eq. (5) can be further decomposed as

$$M_{V\_\mathrm{QR}} = M_{V\_\mathrm{SW}} + M_{V\_\mathrm{SW}} = \alpha\overline{Q_{\mathrm{SW}}} + \alpha\overline{Q_{\mathrm{LW}}}. \qquad (6)$$

Figures 12a–c show the time evolution of the total radiative heating profiles (color shading) and the induced vertical motion anomalies (contours) under diabatic balance. Only the average of the whole BSISO redevelopment region is shown due to the extensive area coverage of ES anvil clouds [>70%, Fig. 10a(3)]. The total radiation, Q_R, manifests largely as cooling throughout the air column (Fig. 12a) due to the strong cooling effect of longwave radiation, Q_{LW} (Fig. 12c), balanced by the weak warming effect of shortwave radiation, Q_{SW} (Fig. 12b). The value of Q_R increases and is deepened from the developing through the early suppressed stages of this BSISO event, which is also attributed largely to Q_{LW} since the variation of Q_{SW} is minor. The strengthening of Q_{LW} is jointly caused by the increase of DS and ES, while the deepening of Q_{LW} is mainly from ES (Fig. 10). As a consequence of the anomalous longwave radiative heating (i.e., the greenhouse warming effect), a compensated upward motion occurs and tilts toward the suppressed stage. Using (5) and (6), we calculate the vertical moisture advection caused by the total radiation M_{V_QR} and its two components M_{V_SW} and M_{V_LW} (Figs. 12d–e). The tilted upward motion also induces tilted column moistening (Fig. 12d), which is explained largely by M_{V_LW} (Fig. 12f). The in-phase relationship between M_{V_LW} and the anomalous moisture implies the positive role of cloud–radiation effects in the maintenance of this BSISO event.

7. Summary and discussion

Despite the extensive documentation of moisture and radiation feedbacks in the dynamics of MJO [see recent reviews by Zhang et al. (2020) and Jiang et al. (2020)], the importance of moisture variability under the influence of clouds is less appreciated and far from established for BSISO. In this study, a high-resolution simulation at the cloud-permitting scale (3 km) from the WRF Model was used to analyze the moisture variation with cloud effects during a BSISO event that redeveloped rapidly from the Sulawesi Sea over the eastern MC. Using an objective cloud-type classification method, we evaluated the column moistening and drying associated with different precipitating and nonprecipitating cloud populations. Cloud–radiation effects were also diagnosed under the WTG

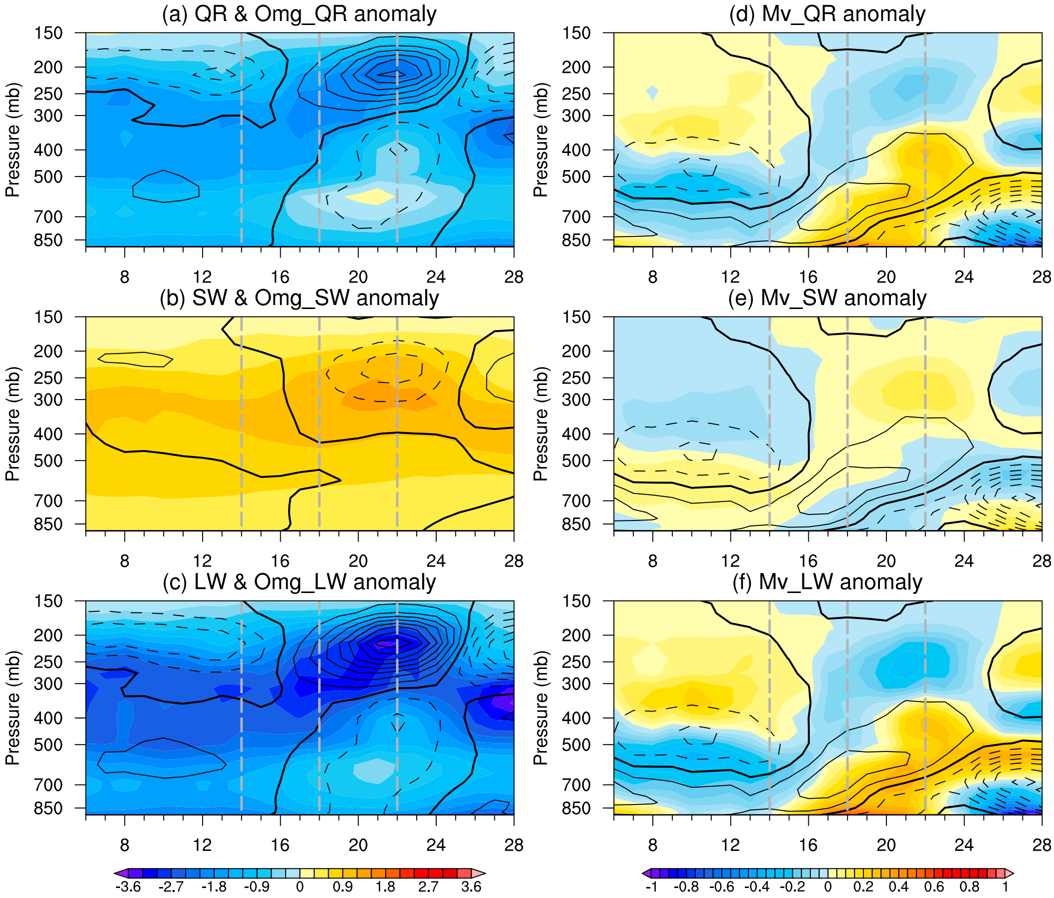

FIG. 12. (a)–(c) Time evolution of the total radiative heating profile (Q_R, shading, K day^{-1}) and the induced anomalous vertical motion (Omg_Q_R, contours, hPa h^{-1}) calculated based on the WTG approximation. The solid (dashed) contours denote the descent (ascent), with an interval of 1 hPa h^{-1}. The zero contours are shown by the thick black line. (d)–(f) Time evolution of anomalous vertical moisture advection induced by total radiative heating (shading, g kg^{-1} day^{-1}) overlaid by the specific humidity anomaly (contours, g kg^{-1}). The contour information is as in Fig. 8. The four BSISO periods are separated by the three vertical dotted lines.

approximation. The main findings are summarized and discussed as follows.

The high-resolution simulation well captures the mean and intraseasonal-scale precipitation and lower-tropospheric winds associated with this BSISO event, as compared with satellite observations and reanalysis products. A close relationship between moisture and precipitation is found for this BSISO case: preceding the onset of deep convection, alternating moistening and drying exist; tropospheric moistening becomes the strongest and deepest immediately preceding the maximal precipitation; accompanied by decreasing precipitation, drying occurs first from the boundary layer and then moves up. Analysis of the total moisture budget from the WRF simulation reveals that the moisture recharge and discharge of this BSISO event are caused mainly by zonal advection, while the role of meridional advection is negligible. According to previous studies (Hsu and Li 2012; Hagos et al. 2014; Sobel et al. 2014; Nasuno et al. 2015; Adames et al. 2016; Zhang and Ling 2017; Hung and Sui 2018; Jiang et al. 2018), the relative importance of zonal versus meridional components in explaining the total horizontal moisture variation of TISO is very changeable, depending on the focus as far as season, geographic region, data, and even analysis method. Column processes are largely in phase with the anomalous moisture, suggesting their critical role in the maintenance of BSISO.

Using the high-resolution simulation, four types of cloud populations are classified over the BSISO redevelopment region, including DC, DS, ES, and SC. Cloud effects are illustrated schematically in Fig. 13, showing the time evolution of the rain rate and rain area fraction (lines in bottom panel), the origination of the cloud population (clusters in top panel), and the variation in the vertical motion (arrows) and anomalous column moistening (red shading) at different stages of BSISO. The rain area fraction of DC, DS, and SC reaches a peak during the mature phase of BSISO deep convection, while that of ES peaks during the transition from the decaying to the suppressed stages of this BSISO event. Column moistening is contributed mainly by ES anvil clouds through the evaporation of cloud water in the lower troposphere. The decrease in DC condensation drying and the reevaporation of DS precipitation also

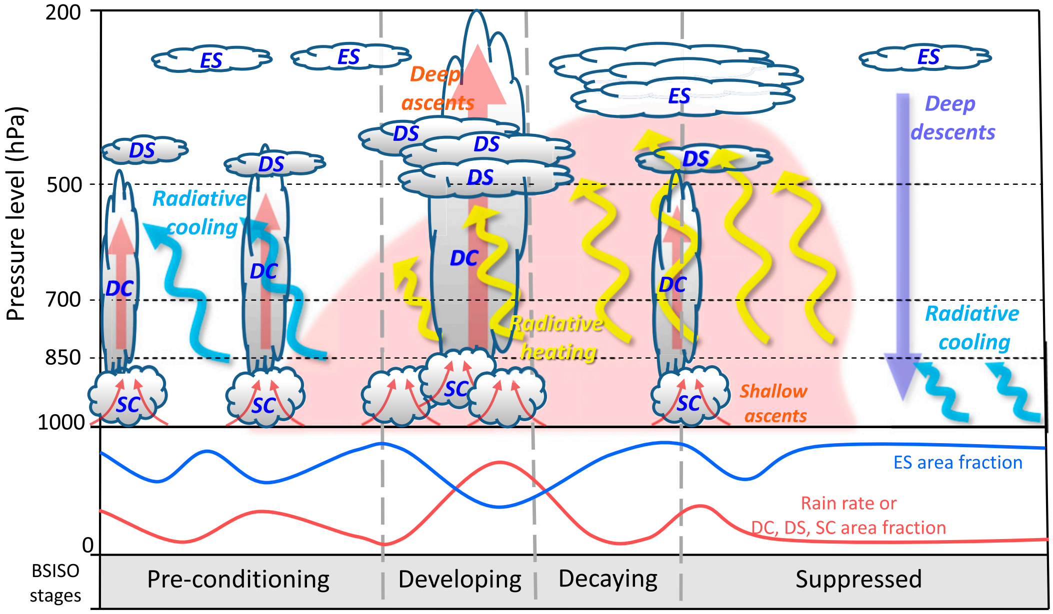

FIG. 13. (top) Schematic diagram illustrating the evolution of cloud populations and column moistening (red background) during different periods of this BSISO event. The overlaid elements include (i) different cloud clusters associated with DC, SC, DS, and ES (see the text marked on the clusters); and (ii) deep (thick red arrows) and shallow (thin red arrows) ascent associated with DC and SC and deep descent (thick blue arrows). The anomalous radiative heating and cooling are represented by the yellow and cyan arrows, respectively. (bottom) The red and blue curves show the time evolution of the rain rate (or area fraction of DC, SC, and DS) and ES area fraction, respectively. The four BSISO stages are labeled in the bottom panel and are separated by the three vertical gray dashed lines.

induce moistening during the developing and after the decay of BSISO deep convection, respectively. The effect of SC is minor, however.

Note that the role of stratiform clouds in this BSISO event is contrary to that in the MJO diagnosed by JZ16, who showed that stratiform clouds acted mainly to dry the column. To explain this discrepancy, we show the time evolution and the mean α profile in this BSISO life cycle in Fig. 14. As we can see, α is smaller than 1 in all stages of BSISO (Fig. 14a). Large (>1) α is found only below ~900 hPa (Fig. 14b), where the turbulent diffusion is dominant and the WTG approximation cannot hold well. The smallness of α throughout the free troposphere has an important implication for the role of stratiform clouds. To explain, we use microphysical condensation ($\overline{c}$) and evaporation ($\overline{e}$). According to Chikira (2014), based on the WTG approximation, the indirect moistening/drying effect induced by the external heating/cooling of ($\overline{c}-\overline{e}$) through vertical advection is $\alpha(\overline{c}-\overline{e})$. Using Eq. (2), the net moistening/drying effect of ($\overline{c}-\overline{e}$) becomes $(\alpha-1)(\overline{c}-\overline{e})$. Because in our case α is always smaller than 1 above 900 hPa, the indirect moistening/drying effect of $\alpha(\overline{c}-\overline{e})$ cannot efficiently overcome the direct drying/moistening of ($\overline{c}-\overline{e}$). In other words, the evaporation (reevaporation) of ES (DS) cloud (rain) water will induce a net moistening rather than drying effect in the lower troposphere in this BSISO event.

To illustrate the cloud–radiation interactions, the anomalous radiative heating and cooling are also shown schematically in Fig. 13 as yellow and blue meandering arrows, respectively. The longwave radiative heating anomaly appears first in the lower troposphere during the developing stage of this BSISO event and is further strengthened and elevated by the joint increase of DS and ES anvil clouds. Responding to this "greenhouse warming effect," a compensated upward motion tilted vertically toward the suppressed period of this BSISO event is induced and causes an anomalous moistening that is largely in phase with intraseasonal-scale humidity through vertical advection. This suggests that cloud–radiation feedback is also important for the maintenance of this BSISO event. Following Chikira (2014), the linearization of (5) with respect to the July mean can further derive the role of the anomalous variation in α in causing moistening and/or drying through the mean radiation. Nevertheless, the cloud–radiation effect was analyzed under a framework of the WTG approximation, which may not be valid in some other cases. Future work should focus on more case studies and use more advanced methods or observations (if available) for in-depth analyses.

Note from Fig. 3 that the zonal mean moisture gradient over the Sulawesi Sea where the BSISO redeveloped rapidly is very weak, which probably implies a negligible role of the zonal advection of mean moisture by intraseasonal-scale wind anomalies. Due to the short duration of the WRF simulation in this study, we utilized long-term ERA5 data to check the scale interactions in total zonal moisture advection (figure not shown). As conjectured, the mean moisture advection due to BSISO zonal wind anomalies did play a minor role in contributing to the total zonal advection, which is quite different

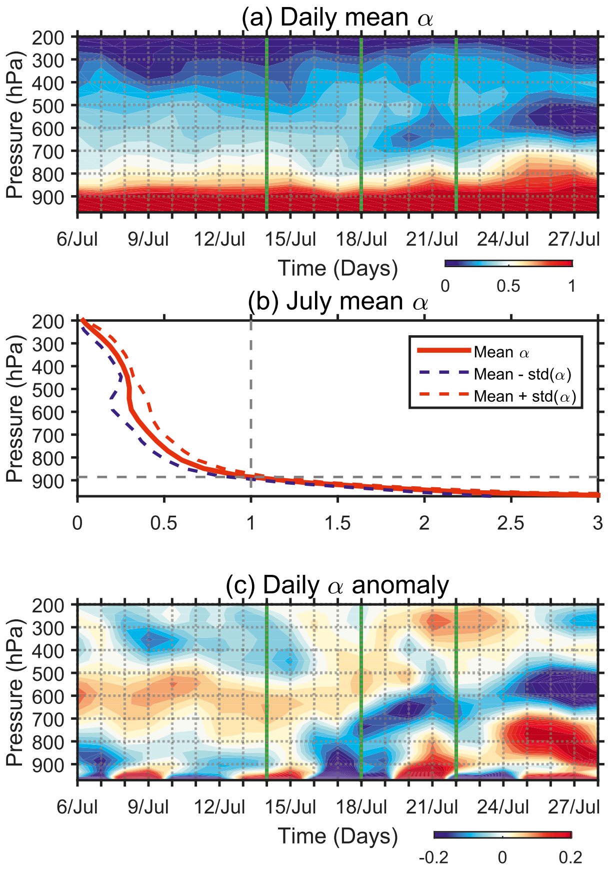

FIG. 14. (a) Time evolution of daily mean α averaged over the BSISO redevelopment region (1°–6°N, 119°–125°E). (b) July-mean α (solid red) and the mean minus (dashed blue) and plus (dashed red) one standard deviation. (c) As in (a), but for the α anomaly relative to the mean α shown in (b). The four BSISO periods are separated by the three vertical green lines in (a) and (c).

from Jiang (2017), who emphasized its dominant role in MJO eastward propagation. This further suggests the key role of the mean state in regulating the moisture variation of MJO/BSISO (Jiang 2017; Jiang et al. 2018). For this BSISO case, however, the dominant term for the total zonal advection in the lower troposphere and boundary layer was diagnosed to be high-frequency moisture transport, which is an important difference in the moistening process over the MC, as compared with other tropical regions.

Some caveats in this study are also worth noting. For example, in deriving the cloud effects through column processes, we did not explicitly isolate the separate role of microphysics and eddy transport, as did Chikira (2014) and JZ16. Instead, we examined the total effect (i.e., M_{ME}). In addition, the individual contribution of different microphysics such as condensation, evaporation, sublimation, and deposition to the tendencies of potential temperature and humidity was not further analyzed either. These issues could be well addressed under the framework of WTG approximation (Chikira 2014) and are left for future study. Furthermore, many studies have argued that the underlying ocean may feed back to TISO [see review by Lau and Waliser (2012) and DeMott et al. (2015)]. However, this potential feedback cannot be represented by only forced atmospheric model simulations. Specifically, we have checked the simulation fidelity of this BSISO event that redeveloped over the Sulawesi Sea using the persistent, daily, and 6-hourly lower boundary conditions of SST, respectively. The strongest rainfall initiation was captured using the 6-h SST, thus implying the potential influence of subdaily-scale air–sea interaction. Therefore, a high-frequency ocean–atmosphere coupled model that can well simulate the intraseasonal variability of the oceanic mixed layer temperature over the Sulawesi Sea is needed in future work.

Acknowledgments. This study is supported by the NOAA Climate Variability and Predictability (CVP) program through Award NA17OAR4310262. The OMI and RMM indexes used in this study have been downloaded from https://psl.noaa.gov/mjo/mjoindex/ and http://www.bom.gov.au/climate/mjo/, respectively. CMORPH data are from https://www.ncei.noaa.gov/data/cmorph-high-resolution-global-precipitation-estimates/. The global ERA5 data are downloaded from https://cds.climate.copernicus.eu/cdsapp#!/dataset/reanalysis-era5-pressure-levels?tab=form. Interpolated OLR data are provided by the NOAA/OAR/ESRL PSL, Boulder, Colorado, from their website at https://psl.noaa.gov/. Early discussion with Dr. Hong-Li Ren (by YW) on large-scale aspects of TISO is acknowledged. We also appreciate three anonymous reviewers for their comments and suggestions that helped improve this paper. Computer support from the Center for High Performance Computing at the University of Utah is acknowledged.

REFERENCES

Adames, Á. F., and D. Kim, 2016: The MJO as a dispersive, convectively coupled moisture wave: Theory and observations. *J. Atmos. Sci.*, **73**, 913–941, https://doi.org/10.1175/JAS-D-15-0170.1.

——, J. M. Wallace, and J. M. Monteiro, 2016: Seasonality of the structure and propagation characteristics of the MJO. *J. Atmos. Sci.*, **73**, 3511–3526, https://doi.org/10.1175/JAS-D-15-0232.1.

Ahn, M. S., D. Kim, K. R. Sperber, I. S. Kang, E. Maloney, D. Waliser, and H. Hendon, 2017: MJO simulation in CMIP5 climate models: MJO skill metrics and process-oriented diagnosis. *Climate Dyn.*, **49**, 4023–4045, https://doi.org/10.1007/s00382-017-3558-4.

Andersen, J. A., and Z. Kuang, 2012: Moist static energy budget of MJO-like disturbances in the atmosphere of a zonally symmetric aquaplanet. *J. Climate*, **25**, 2782–2804, https://doi.org/10.1175/JCLI-D-11-00168.1.

Bellenger, H., K. Yoneyama, M. Katsumata, T. Nishizawa, K. Yasunaga, and R. Shirooka, 2015: Observation of moisture tendencies related to shallow convection. *J. Atmos. Sci.*, **72**, 641–659, https://doi.org/10.1175/JAS-D-14-0042.1.

Benedict, J. J., and D. A. Randall, 2007: Observed characteristics of the MJO relative to maximum rainfall. *J. Atmos. Sci.*, **64**, 2332–2354, https://doi.org/10.1175/JAS3968.1.

Bladé, I., and D. L. Hartmann, 1993: Tropical intraseasonal oscillations in a simple nonlinear model. *J. Atmos. Sci.*, **50**, 2922–2939, https://doi.org/10.1175/1520-0469(1993)050<2922:TIOIAS>2.0.CO;2.

Chen, S. S., and R. A. Houze Jr., 1997: Diurnal variation and life cycle of deep convective systems over the tropical Pacific warm pool. *Quart. J. Roy. Meteor. Soc.*, **123**, 357–388, https://doi.org/10.1002/qj.49712353806.

Chikira, M., 2014: Eastward-propagating intraseasonal oscillation represented by Chikira–Sugiyama cumulus parameterization. Part II: Understanding moisture variation under weak temperature gradient balance. *J. Atmos. Sci.*, **71**, 615–639, https://doi.org/10.1175/JAS-D-13-038.1.

Churchill, D. D., and R. A. Houze Jr., 1984: Development and structure of winter monsoon cloud clusters on 10 December 1978. *J. Atmos. Sci.*, **41**, 933–960, https://doi.org/10.1175/1520-0469(1984)041<0933:DASOWM>2.0.CO;2.

DeMott, C. A., C. Stan, and D. A. Randall, 2013: Northward propagation mechanisms of the boreal summer intraseasonal oscillation in the ERA-Interim and SP-CCSM. *J. Climate*, **26**, 1973–1992, https://doi.org/10.1175/JCLI-D-12-00191.1.

——, N. P. Klingaman, and S. J. Woolnough, 2015: Atmosphere-ocean coupled processes in the Madden-Julian oscillation. *Rev. Geophys.*, **53**, 1099–1154, https://doi.org/10.1002/2014RG000478.

Fabry, F., I. Zawadzki, and S. Cohn, 1993: The influence of stratiform precipitation on shallow convective rain: A case study. *Mon. Wea. Rev.*, **121**, 3312–3325, https://doi.org/10.1175/1520-0493(1993)121<3312:TIOSPO>2.0.CO;2.

Funk, A., C. Schumacher, and J. Awaka, 2013: Analysis of rain classifications over the tropics by version 7 of the TRMM PR 2A23 algorithm. *J. Meteor. Soc. Japan*, **91**, 257–272, https://doi.org/10.2151/jmsj.2013-302.

Gill, A. E., 1980: Some simple solutions for heat-induced tropical circulation. *Quart. J. Roy. Meteor. Soc.*, **106**, 447–462, https://doi.org/10.1002/qj.49710644905.

Haertel, P. T., G. N. Kiladis, A. Denno, and T. M. Rickenbach, 2008: Vertical-mode decompositions of 2-day waves and the Madden–Julian oscillation. *J. Atmos. Sci.*, **65**, 813–833, https://doi.org/10.1175/2007JAS2314.1.

Hagos, S., Z. Feng, K. Landu, and C. N. Long, 2014: Advection, moistening, and shallow-to-deep convection transitions during the initiation and propagation of Madden-Julian oscillation. *J. Adv. Model. Earth Syst.*, **6**, 938–949, https://doi.org/10.1002/2014MS000335.

——, and Coauthors, 2016: The impact of the diurnal cycle on the propagation of Madden-Julian oscillation convection across the Maritime Continent. *J. Adv. Model. Earth Syst.*, **8**, 1552–1564, https://doi.org/10.1002/2016MS000725.

Handlos, Z. J., and L. E. Back, 2014: Estimating vertical motion profile shape within tropical weather states over the oceans. *J. Climate*, **27**, 7667–7686, https://doi.org/10.1175/JCLI-D-13-00602.1.

Hendon, H. H., and M. L. Salby, 1994: The life cycle of the Madden–Julian oscillation. *J. Atmos. Sci.*, **51**, 2225–2237, https://doi.org/10.1175/1520-0469(1994)051<2225:TLCOTM>2.0.CO;2.

Hersbach, H., and Coauthors, 2020: The ERA5 global reanalysis. *Quart. J. Roy. Meteor. Soc.*, **146**, 1999–2049, https://doi.org/10.1002/qj.3803.

Hohenegger, C., and B. Stevens, 2013: Preconditioning deep convection with cumulus congestus. *J. Atmos. Sci.*, **70**, 448–464, https://doi.org/10.1175/JAS-D-12-089.1.

Houze, R. A., Jr., 1997: Stratiform precipitation in regions of convection: A meteorological paradox? *Bull. Amer. Meteor. Soc.*, **78**, 2179–2196, https://doi.org/10.1175/1520-0477(1997)078<2179:SPIROC>2.0.CO;2.

Hsu, P. C., and T. Li, 2012: Role of the boundary layer moisture asymmetry in causing the eastward propagation of the Madden–Julian oscillation. *J. Climate*, **25**, 4914–4931, https://doi.org/10.1175/JCLI-D-11-00310.1.

Hu, Q., and D. A. Randall, 1994: Low-frequency oscillations in radiative–convective systems. *J. Atmos. Sci.*, **51**, 1089–1099, https://doi.org/10.1175/1520-0469(1994)051<1089:LFOIRC>2.0.CO;2.

Hung, C. S., and C. H. Sui, 2018: A diagnostic study of the evolution of the MJO from Indian Ocean to Maritime Continent: Wave dynamics versus advective moistening processes. *J. Climate*, **31**, 4095–4115, https://doi.org/10.1175/JCLI-D-17-0139.1.

Inoue, K., Á. F. Adames, and K. Yasunaga, 2020: Vertical velocity profiles in convectively coupled equatorial waves and MJO: New diagnoses of vertical velocity profiles in the wavenumber–frequency domain. *J. Atmos. Sci.*, **77**, 2139–2162, https://doi.org/10.1175/JAS-D-19-0209.1.

Janiga, M. A., and C. Zhang, 2016: MJO moisture budget during DYNAMO in a cloud-resolving model. *J. Atmos. Sci.*, **73**, 2257–2278, https://doi.org/10.1175/JAS-D-14-0379.1.

Jiang, X., 2017: Key processes for the eastward propagation of the Madden-Julian oscillation based on multimodal simulations. *J. Geophys. Res. Atmos.*, **122**, 755–770, https://doi.org/10.1002/2016JD025955.

——, T. Li, and B. Wang, 2004: Structures and mechanisms of the northward propagating boreal summer intraseasonal oscillation. *J. Climate*, **17**, 1022–1039, https://doi.org/10.1175/1520-0442(2004)017<1022:SAMOTN>2.0.CO;2.

——, and Coauthors, 2015: Vertical structure and physical processes of the Madden-Julian oscillation: Exploring key model physics in climate simulations. *J. Geophys. Res. Atmos.*, **120**, 4718–4748, https://doi.org/10.1002/2014JD022375.

——, Á. F. Adames, M. Zhao, D. Waliser, and E. Maloney, 2018: A unified moisture mode framework for seasonality of the Madden–Julian oscillation. *J. Climate*, **31**, 4215–4224, https://doi.org/10.1175/JCLI-D-17-0671.1.

——, and Coauthors, 2020: Fifty years of research on the Madden-Julian oscillation: Recent progress, challenges, and perspectives. *J. Geophys. Res. Atmos.*, **125**, e2019JD030911, https://doi.org/10.1029/2019JD030911.

Johnson, R. H., and P. E. Ciesielski, 2013: Structure and properties of Madden–Julian oscillations deduced from DYNAMO sounding arrays. *J. Atmos. Sci.*, **70**, 3157–3179, https://doi.org/10.1175/JAS-D-13-065.1.

——, T. M. Rickenbach, S. A. Rutledge, P. E. Ciesielski, and W. H. Schubert, 1999: Trimodal characteristics of tropical convection. *J. Climate*, **12**, 2397–2418, https://doi.org/10.1175/1520-0442(1999)012<2397:TCOTC>2.0.CO;2.

Joyce, R. J., J. E. Janowiak, P. A. Arkin, and P. Xie, 2004: CMORPH: A method that produces global precipitation estimates from passive microwave and infrared data at high spatial and temporal resolution. *J. Hydrol.*, **5**, 487–503, https://doi.org/10.1175/1525-7541(2004)005<0487:CAMTPG>2.0.CO;2.

Kemball-Cook, S. R., and B. C. Weare, 2001: The onset of convection in the Madden–Julian oscillation. *J. Climate*, **14**, 780–793, https://doi.org/10.1175/1520-0442(2001)014<0780:TOOCIT>2.0.CO;2.

Kikuchi, K., B. Wang, and Y. Kajikawa, 2012: Bimodal representation of the tropical intraseasonal oscillation. *Climate Dyn.*, **38**, 1989–2000, https://doi.org/10.1007/s00382-011-1159-1.

Kiladis, G. N., K. H. Straub, and P. T. Haertel, 2005: Zonal and vertical structure of the Madden–Julian oscillation. *J. Atmos. Sci.*, **62**, 2790–2809, https://doi.org/10.1175/JAS3520.1.

——, M. C. Wheeler, P. T. Haertel, K. H. Straub, and P. E. Roundy, 2009: Convectively coupled equatorial waves. *Rev. Geophys.*, **47**, RG2003, https://doi.org/10.1029/2008RG000266.

——, J. Dias, K. H. Straub, M. C. Wheeler, S. N. Tulich, K. Kikuchi, K. M. Weickmann, and M. J. Ventrice, 2014: A comparison of OLR and circulation-based indices for tracking the MJO. *Mon. Wea. Rev.*, **142**, 1697–1715, https://doi.org/10.1175/MWR-D-13-00301.1.

Kim, D., M. S. Ahn, I. S. Kang, and A. D. Del Genio, 2015: Role of longwave cloud–radiation feedback in the simulation of the Madden–Julian oscillation. *J. Climate*, **28**, 6979–6994, https://doi.org/10.1175/JCLI-D-14-00767.1.

Krishnamurti, T. N., and D. Subramanian, 1982: The 30-50 day mode at 850 mb during MONEX. *J. Atmos. Sci.*, **39**, 2088–2095, https://doi.org/10.1175/1520-0469(1982)039<2088:TDMAMD>2.0.CO;2.

Kuang, Z., 2008: A moisture-stratiform instability for convectively coupled waves. *J. Atmos. Sci.*, **65**, 834–854, https://doi.org/10.1175/2007JAS2444.1.

Kubota, H., K. Yoneyama, J. I. Hamada, P. Wu, A. Sudaryanto, and I. B. Wahyono, 2015: Role of Maritime Continent convection during the preconditioning stage of the Madden-Julian oscillation observed in CINDY2011/DYNAMO. *J. Meteor. Soc. Japan*, **93A**, 101–114, https://doi.org/10.2151/JMSJ.2015-050.

Kumar, V. V., C. Jako, A. Protat, P. T. May, and L. Davies, 2013: The four cumulus cloud modes and their progression during rainfall events: AC-band polarimetric radar perspective. *J. Geophys. Res. Atmos.*, **118**, 8375–8389, https://doi.org/10.1002/jgrd.50640.

Lau, W. K. M., and D. E. Waliser, 2012: *Intraseasonal Variability in the Atmosphere-Ocean Climate System*. Springer Science and Business Media, 437 pp.

Lee, M.-I., I.-S. Kang, J.-K. Kim, and B. E. Mapes, 2001: Influence of cloud-radiation interaction on simulating tropical intraseasonal oscillation with an atmospheric general circulation model. *J. Geophys. Res.*, **106**, 14 219–14 233, https://doi.org/10.1029/2001JD900143.

Li, T., and C. Zhou, 2009: Planetary scale selection of the Madden–Julian oscillation. *J. Atmos. Sci.*, **66**, 2429–2443, https://doi.org/10.1175/2009JAS2968.1.

Liebmann, B., and C. A. Smith, 1996: Description of a complete (interpolated) outgoing longwave radiation dataset. *Bull. Amer. Meteor. Soc.*, **77**, 1275–1277, https://doi.org/10.1175/1520-0477-77.6.1274.

Madden, R. A., and P. R. Julian, 1971: Detection of a 40–50 day oscillation in the zonal wind in the tropical Pacific. *J. Atmos. Sci.*, **28**, 702–708, https://doi.org/10.1175/1520-0469(1971)028<0702:DOADOI>2.0.CO;2.

——, and ——, 1972: Description of global-scale circulation cells in the tropics with a 40–50 day period. *J. Atmos. Sci.*, **29**, 1109–1123, https://doi.org/10.1175/1520-0469(1972)029<1109:DOGSCC>2.0.CO;2.

Maloney, E. D., 2009: The moist static energy budget of a composite tropical intraseasonal oscillation in a climate model. *J. Climate*, **22**, 711–729, https://doi.org/10.1175/2008JCLI2542.1.

Mapes, B. E., 2000: Convective inhibition, subgrid-scale triggering energy, and stratiform instability in a toy tropical wave model. *J. Atmos. Sci.*, **57**, 1515–1535, https://doi.org/10.1175/1520-0469(2000)057<1515:CISSTE>2.0.CO;2.

——, S. Tulich, J. Lin, and P. Zuidema, 2006: The mesoscale convection life cycle: Building block or prototype for large-scale tropical waves? *Dyn. Atmos. Oceans*, **42**, 3–29, https://doi.org/10.1016/j.dynatmoce.2006.03.003.

Matthews, A. J., 2008: Primary and successive events in the Madden–Julian oscillation. *Quart. J. Roy. Meteor. Soc.*, **134**, 439–453, https://doi.org/10.1002/qj.224.

Mei, S., T. Li, and W. Chen, 2015: Three-type MJO initiation processes over the western equatorial Indian Ocean. *Adv. Atmos. Sci.*, **32**, 1208–1216, https://doi.org/10.1007/s00376-015-4201-0.

Nasuno, T., T. Li, and K. Kikuchi, 2015: Moistening processes before the convective initiation of Madden–Julian oscillation events during the CINDY2011/DYNAMO period. *Mon. Wea. Rev.*, **143**, 622–643, https://doi.org/10.1175/MWR-D-14-00132.1.

Neena, J. M., J. Y. Lee, D. Waliser, B. Wang, and X. Jiang, 2014: Predictability of the Madden–Julian oscillation in the Intraseasonal Variability Hindcast Experiment (ISVHE). *J. Climate*, **27**, 4531–4543, https://doi.org/10.1175/JCLI-D-13-00624.1.

Parker, M. D., and R. H. Johnson, 2004: Structures and dynamics of quasi-2D mesoscale convective systems. *J. Atmos. Sci.*, **61**, 545–567, https://doi.org/10.1175/1520-0469(2004)061<0545:SADOQM>2.0.CO;2.

Powell, S. W., and R. A. Houze Jr., 2013: The cloud population and onset of the Madden-Julian oscillation over the Indian Ocean during DYNAMO-AMIE. *J. Geophys. Res. Atmos.*, **118**, 11 979–11 995, https://doi.org/10.1002/2013JD020421.

——, and ——, 2015: Effect of dry large-scale vertical motions on initial MJO convective onset. *J. Geophys. Res. Atmos.*, **120**, 4783–4805, https://doi.org/10.1002/2014JD022961.

Reynolds, R. W., and Coauthors, 2007: Daily high-resolution-blended analyses for sea surface temperature. *J. Climate*, **20**, 5473–5496, https://doi.org/10.1175/2007JCLI1824.1.

Ricko, M., R. F. Adler, and G. J. Huffman, 2016: Climatology and interannual variability of quasi-global intense precipitation using satellite observations. *J. Climate*, **29**, 5447–5468, https://doi.org/10.1175/JCLI-D-15-0662.1.

Roundy, P. E., C. J. Schreck III, and M. A. Janiga, 2009: Contributions of convectively coupled equatorial Rossby waves and Kelvin waves to the real-time multivariate MJO indices. *Mon. Wea. Rev.*, **137**, 469–478, https://doi.org/10.1175/2008MWR2595.1.

Rowe, A. K., and R. A. Houze, 2014: Microphysical characteristics of MJO convection over the Indian Ocean during DYNAMO. *J. Geophys. Res. Atmos.*, **119**, 2543–2554, https://doi.org/10.1002/2013JD020799.

Ruppert, J. H., Jr., and F. Zhang, 2019: Diurnal forcing and phase locking of gravity waves in the Maritime Continent. *J. Atmos. Sci.*, **76**, 2815–2835, https://doi.org/10.1175/JAS-D-19-0061.1.

——, X. Chen, and F. Zhang, 2020: Convectively forced diurnal gravity waves in the Maritime Continent. *J. Atmos. Sci.*, **77**, 1119–1136, https://doi.org/10.1175/JAS-D-19-0236.1.

Sabeerali, C. T., A. Ramu Dandi, A. Dhakat, K. Salunke, S. Mahapatra, and S. A. Rao, 2013: Simulation of boreal summer intraseasonal oscillations in the latest CMIP5 coupled GCMs. *J. Geophys. Res. Atmos.*, **118**, 4401–4420, https://doi.org/10.1002/jgrd.50403.

Schumacher, C., R. A. Houze Jr., and I. Kraucunas, 2004: The tropical dynamical response to latent heating estimates derived from the TRMM Precipitation Radar. *J. Atmos. Sci.*, **61**, 1341–1358, https://doi.org/10.1175/1520-0469(2004)061<1341:TTDRTL>2.0.CO;2.

——, M. H. Zhang, and P. E. Ciesielski, 2007: Heating structures of the TRMM field campaigns. *J. Atmos. Sci.*, **64**, 2593–2610, https://doi.org/10.1175/JAS3938.1.

Seo, K. H. and K. Y. Kim, 2003: Propagation and initiation mechanisms of the Madden-Julian oscillation. *J. Geophys. Res.*, **108**, 4384, https://doi.org/10.1029/2002JD002876.

Shige, S., Y. N. Takayabu, W. K. Tao, and D. E. Johnson, 2004: Spectral retrieval of latent heating profiles from TRMM PR data. Part I: Development of a model-based algorithm. *J. Appl. Meteor.*, **43**, 1095–1113, https://doi.org/10.1175/1520-0450(2004)043<1095:SROLHP>2.0.CO;2.

Skamarock, W. C., and Coauthors, 2019: A description of the Advanced Research WRF Model version 4. NCAR Tech. Note NCAR/TN-556+STR, 145 pp., https://doi.org/10.5065/1dfh-6p97.

Sobel, A. H., J. Nilsson, and L. M. Polvani, 2001: The weak temperature gradient approximation and balanced tropical moisture waves. *J. Atmos. Sci.*, **58**, 3650–3665, https://doi.org/10.1175/1520-0469(2001)058<3650:TWTGAA>2.0.CO;2.

——, S. Waang, and D. Kim, 2014: Moist static energy budget of the MJO during DYNAMO. *J. Atmos. Sci.*, **71**, 4276–4291, https://doi.org/10.1175/JAS-D-14-0052.1.

Storm, B. A., M. D. Parker, and D. P. Jorgensen, 2007: A convective line with leading stratiform precipitation from BAMEX. *Mon. Wea. Rev.*, **135**, 1769–1785, https://doi.org/10.1175/MWR3392.1.

Straub, K. H., 2013: MJO initiation in the real-time multivariate MJO index. *J. Climate*, **26**, 1130–1151, https://doi.org/10.1175/JCLI-D-12-00074.1.

Tao, W. K., and Coauthors, 1993: Heating, moisture, and water budgets of tropical and midlatitude squall lines: Comparisons and sensitivity to longwave radiation. *J. Atmos. Sci.*, **50**, 673–690, https://doi.org/10.1175/1520-0469(1993)050<0673:HMAWBO>2.0.CO;2.

Tulich, S. N., and G. N. Kiladis, 2012: Squall lines and convectively coupled gravity waves in the tropics: Why do most cloud systems propagate westward? *J. Atmos. Sci.*, **69**, 2995–3012, https://doi.org/10.1175/JAS-D-11-0297.1.

Vincent, C. L., and T. P. Lane, 2016: Evolution of the diurnal precipitation cycle with the passage of a Madden–Julian oscillation event through the Maritime Continent. *Mon. Wea. Rev.*, **144**, 1983–2005, https://doi.org/10.1175/MWR-D-15-0326.1.

——, and ——, 2018: Mesoscale variation in diabatic heating around Sumatra, and its modulation with the Madden–Julian oscillation. *Mon. Wea. Rev.*, **146**, 2599–2614, https://doi.org/10.1175/MWR-D-17-0392.1.

Wang, B., and X. Xie, 1997: A model for the boreal summer intraseasonal oscillation. *J. Atmos. Sci.*, **54**, 72–86, https://doi.org/10.1175/1520-0469(1997)054<0072:AMFTBS>2.0.CO;2.

Wang, S., A. H. Sobel, and Z. Kuang, 2013: Cloud-resolving simulation of TOGA-COARE using parameterized large-scale dynamics. *J. Geophys. Res. Atmos.*, **118**, 6290–6301, https://doi.org/10.1002/jgrd.50510.

——, ——, and J. Nie, 2016: Modeling the MJO in a cloud-resolving model with parameterized large-scale dynamics: Vertical structure, radiation, and horizontal advection of dry air. *J. Adv. Model. Earth Syst.*, **8**, 121–139, https://doi.org/10.1002/2015MS000529.

——, D. Ma, A. H. Sobel, and M. K. Tippett, 2018: Propagation characteristics of BSISO indices. *Geophys. Res. Lett.*, **45**, 9934–9943, https://doi.org/10.1029/2018GL078321.

——, A. H. Sobel, M. K. Tippett, and F. Vitart, 2019: Prediction and predictability of tropical intraseasonal convection: Seasonal dependence and the Maritime Continent prediction barrier. *Climate Dyn.*, **52**, 6015–6031, https://doi.org/10.1007/s00382-018-4492-9.

Wei, Y., F. Liu, M. Mu, and H. L. Ren, 2018: Planetary scale selection of the Madden–Julian oscillation in an air-sea coupled dynamic moisture model. *Climate Dyn.*, **50**, 3441–3456, https://doi.org/10.1007/s00382-017-3816-5.

——, M. Mu, H.-L. Ren, and J.-X. Fu, 2019a: Conditional nonlinear optimal perturbations of moisture triggering primary MJO initiation. *Geophys. Res. Lett.*, **46**, 3492–3501, https://doi.org/10.1029/2018GL081755.

——, F. Liu, M. Mu, and H. L. Ren, 2019b: Modulation of ENSO on fast and slow MJO modes during boreal winter. *J. Climate*, **32**, 7483–7506, https://doi.org/10.1175/JCLI-D-19-0013.1.

——, ——, ——, and ——, 2020a: Nonlinear optimal moisture perturbations as excitation of primary MJO events in a hybrid coupled climate model. *Climate Dyn.*, **54**, 675–699, https://doi.org/10.1007/s00382-019-05021-7.

——, Z. Pu, and C. Zhang, 2020b: Diurnal cycle of precipitation over the Maritime Continent under modulation of MJO: Perspectives from a cloud-permitting simulation. *J. Geophys. Res. Atmos.*, **125**, e2020JD032529, https://doi.org/10.1029/2020JD032529.

Wheeler, M., and H. H. Hendon, 2004: An all-season real-time multivariate MJO index: Development of an index for monitoring and prediction. *Mon. Wea. Rev.*, **132**, 1917–1932, https://doi.org/10.1175/1520-0493(2004)132<1917:AARMMI>2.0.CO;2.

Xu, W., and S. A. Rutledge, 2014: Convective characteristics of the Madden–Julian oscillation over the central Indian Ocean observed by shipborne radar during DYNAMO. *J. Atmos. Sci.*, **71**, 2859–2877, https://doi.org/10.1175/JAS-D-13-0372.1.

——, and ——, 2016: Time scales of shallow-to-deep convective transition associated with the onset of Madden-Julian oscillations. *Geophys. Res. Lett.*, **43**, 2880–2888, https://doi.org/10.1002/2016GL068269.

Yanai, M., S. Esbensen, and J. H. Chu, 1973: Determination of bulk properties of tropical cloud clusters from large-scale heat and moisture budgets. *J. Atmos. Sci.*, **30**, 611–627, https://doi.org/10.1175/1520-0469(1973)030<0611:DOBPOT>2.0.CO;2.

Yang, Y. M., J. Y. Lee, and B. Wang, 2020: Dominant process for northward propagation of boreal summer intraseasonal oscillation over the western North Pacific. *Geophys. Res. Lett.*, **47**, e2020GL089808, https://doi.org/10.1029/2020GL089808.

Yano, J. I., and M. Bonazzola, 2009: Scale analysis for large-scale tropical atmospheric dynamics. *J. Atmos. Sci.*, **66**, 159–172, https://doi.org/10.1175/2008JAS2687.1.

Yasunari, T., 1979: Cloudiness fluctuations associated with the Northern Hemisphere summer monsoon. *J. Meteor. Soc. Japan*, **57**, 227–242, https://doi.org/10.2151/jmsj1965.57.3_227.

Yokoi, S., and A. H. Sobel, 2015: Intraseasonal variability and seasonal march of the moist static energy budget over the eastern Maritime Continent during CINDY2011/DYNAMO. *J. Meteor. Soc. Japan*, **93A**, 81–100, https://doi.org/10.2151/jmsj.2015-041.

Zermeño-Díaz, D. M., C. Zhang, P. Kollias, and H. Kalesse, 2015: The role of shallow cloud moistening in MJO and non-MJO convective events over the ARM Manus site. *J. Atmos. Sci.*, **72**, 4797–4820, https://doi.org/10.1175/JAS-D-14-0322.1.

Zhang, C., 2005: Madden-Julian oscillation. *Rev. Geophys.*, **43**, RG2003, https://doi.org/10.1029/2004RG000158.

——, 2013: Madden–Julian oscillation: Bridging weather and climate. *Bull. Amer. Meteor. Soc.*, **94**, 1849–1870, https://doi.org/10.1175/BAMS-D-12-00026.1.

——, and S. M. Hagos, 2009: Bi-modal structure and variability of large-scale diabatic heating in the tropics. *J. Atmos. Sci.*, **66**, 3621–3640, https://doi.org/10.1175/2009JAS3089.1.

——, and J. Ling, 2017: Barrier effect of the Indo-Pacific Maritime Continent on the MJO: Perspectives from tracking MJO precipitation. *J. Climate*, **30**, 3439–3459, https://doi.org/10.1175/JCLI-D-16-0614.1.

——, and K. Yoneyama, 2017: CINDY/DYNAMO field campaign: Advancing our understanding of MJO initiation. *The Global Monsoon System: Research and Forecast*, World Scientific, 339–348.

——, A. F. Adames, B. Khouider, B. Wang, and D. Yang, 2020: Four theories of the Madden-Julian oscillation. *Rev. Geophys.*, **58**, e2019RG000685, https://doi.org/10.1029/2019RG000685.